Understanding the geodetic signature of large aquifer systems: Example of the Ozark Plateaus in Central United States

Stacy Larochelle[1], Kristel Chanard[2,3], Luce Fleitout[4], Jérome Fortin[5], Adriano Gualandi[1,6], Laurent Longuevergne[7], Paul Rebischung[2,3], Sophie Violette[4,8], and Jean-Philippe Avouac[1]

[1]Geological and Planetary Sciences, California Institute of Technology, Pasadena, California, USA
[2]Université de Paris, Institut de physique du globe de Paris, CNRS, IGN, Paris, France
[3]ENSG-Géomatique, IGN, Marne-la-Vallée, France
[4]Laboratoire de Géologie, École Normale Supérieure, Université PSL, CNRS, Paris, France
[5]University PSL, CNRS UMR 8538, Paris, France
[6]Istituto Nazionale di Geofisica e Vulcanologia, Osservatorio Nazionale Terremoti, Rome, Italy
[7]Univ Rennes, CNRS, Geosciences Rennes - UMR 6118, F-35000 Rennes, France
[8]Sorbonne University, UFR.918, Paris, France

Key Points:

- We characterize seasonal and multiannual groundwater fluctuations with an Independent Component Analysis.
- We separate and model the hydrological loading and poroelastic deformation fields captured by GNSS.
- We infer relatively low elastic moduli from the extracted poroelastic displacements and groundwater fluctuations.

Corresponding author: Stacy Larochelle, stacy.larochelle@caltech.edu

Abstract

The continuous redistribution of water involved in the hydrologic cycle leads to deformation of the solid Earth. On a global scale, this deformation is well explained by the loading imposed by hydrological mass variations and can be quantified to first order with space-based gravimetric and geodetic measurements. At the regional scale, however, aquifer systems also undergo poroelastic deformation in response to groundwater fluctuations. Disentangling these related but distinct 3D deformation fields from geodetic time series is essential to accurately invert for changes in continental water mass, to understand the mechanical response of aquifers to internal pressure changes as well as to correct time series for these known effects. Here, we demonstrate a methodology to accomplish this task by considering the example of the well-instrumented Ozark Plateaus Aquifer System (OPAS) in central United States. We begin by characterizing the most important sources of groundwater level variations in the spatially heterogeneous piezometer dataset using an Independent Component Analysis. Then, to estimate the associated poroelastic displacements, we project geodetic time series corrected for hydrological loading effects onto the dominant groundwater temporal functions. We interpret the extracted displacements in light of analytical solutions and a 2D model relating groundwater level variations to surface displacements. In particular, the relatively low estimates of elastic moduli inferred from the poroelastic displacements and groundwater fluctuations may be indicative of aquifer layers with a high fracture density. Our findings suggest that OPAS undergoes significant poroelastic deformation, including highly heterogeneous horizontal poroelastic displacements.

Plain Language Summary

A number of hydrological processes can deform the solid Earth. Measuring this deformation through space-based geodesy offers an opportunity to study these hydrologic processes and infer properties of the sub-surface. In the case of an aquifer, surface displacements can arise from changes in total water mass, which load the Earth, as well as from changes in groundwater pressure which alter stresses in the aquifer and in the surrounding medium. In this study, we describe a methodology to extract and separate these distinct but related deformation signals from GNSS time series and hence infer mechanical properties of the aquifer system by using satellite gravimetry data, local groundwater level measurements as well as a blind source separation technique. We also present a mathematical framework to study surface displacements resulting from variations in groundwater pressure in a medium with heterogeneous elastic properties. We demonstrate the methodology in the Ozark Plateaus Aquifer System in central United States.

1 Introduction

Hydrological processes occurring at the surface of the Earth redistribute continental water mass and the resulting load variations deform the solid Earth. The primarily seasonal deformation can be measured with space-based geodetic techniques such as GNSS (Global Navigation Satellite System)(Blewitt et al., 2001; van Dam et al., 2001; Dong et al., 2002). It is thus possible to infer fluctuations in continental water storage from GNSS time series (Ouellette et al., 2013; Argus et al., 2014, 2017; Borsa et al., 2014; Fu et al., 2015; Adusumilli et al., 2019; Ferreira et al., 2019) assuming that the regional deformation field induced by hydrology can be separated from other geodetic signals and/or systematic errors (Chanard et al., 2020). Such regional-scale constraints on hydrological fluctuations help bridge the gap between *in situ* measurements (e.g., groundwater monitoring wells, stream gauges) and continental-scale observations from the Gravity Recovery and Climate Experiment (GRACE) mission (Tapley et al., 2004).

At a global scale, seasonal signals in GNSS time series are not entirely explained by GRACE-measured hydrological loading (Chanard et al., 2018). Additional deformation mechanisms related to groundwater and temperature variations are thought to explain a significant fraction of this seasonal variance (Tsai, 2011). In particular, aquifer basins - which store roughly 30% of Earth's freshwater reserves (Shiklomanov, 1993) - are prone to poroelastic swelling in addition to hydrological loading (Wang, 2000). An increase in surface and groundwater mass (Figure 1A) translates to an increase of load which leads to subsidence and horizontal displacements towards the added load (Boussinesq, 1885; Verruijt, 2009) (Figure 1B). At the same time, the increase in groundwater storage rises pore pressure levels and generates eigenstrains within the aquifer and hence induces uplift and radially outward surface displacements (King et al., 2007; Galloway & Burbey, 2011) (Figure 1C).

Separating the contributions of hydrological loading and poroelasticity in geodetic time series is crucial to better understand the physics of either deformation processes and quantify fluctuations in total water storage. Extracting the poroelastic deformation field has direct implications for inferring, at the field scale, the hydromechanical properties of aquifer systems which are tightly linked to hydrodynamical properties. Indeed, surface deformation provides information about internal aquifer processes which are generally not accessible otherwise. Such insight could improve the representation of groundwater within global and regional hydrological models and hence strengthen their predictive ability (Gleeson et al., 2021). Estimates of effective elastic moduli obtained through geodesy also provide measurements at a scale and loading rate (i.e., quasi-static) relevant for geohydrologic processes and complementary to those obtained through seismology and laboratory experiments (Carlson et al., 2020). Beyond hydrological applications, characterizing the seasonal content of geodetic time series is also essential to isolate the deformation associated with tectonic processes (Michel et al., 2019; Vergnolle et al., 2010) and to investigate the response of seismicity to seasonal forcings (Bettinelli et al., 2008; Craig et al., 2017; C. W. Johnson et al., 2017).

A number of studies, mostly using Interferometric Synthetic Aperture Radar (InSAR), have demonstrated the feasibility of documenting aquifer dynamics and inferring their mechanical properties based on remote sensing measurements of surface deformation and *in situ* measurements of groundwater levels (Amelung et al., 1999; Bell et al., 2008; Wisely & Schmidt, 2010; Galloway & Burbey, 2011; Chaussard et al., 2014, 2017; Miller et al., 2017; Ojha et al., 2018; Riel et al., 2018; Alghamdi et al., 2020; Hu & Bürgmann, 2020; Gualandi & Liu, 2021). Most of these studies focused on aquifer basins where the poroelastic response dominates the local deformation field. At a regional scale, however, both deformation fields vary spatially and are not easily separated given the codependency of these deformation processes.

Here, we describe a new methodology to extract poroelastic deformation from GNSS time series by harnessing observations from the GRACE satellites and *in situ* groundwater monitoring wells as well as a blind source separation technique (Gualandi et al., 2016). Focusing on GNSS data as opposed to InSAR provides (1) a complementary set of geodetic observations with different systematic errors, (2) the opportunity to study larger aquifer systems at which InSAR processing becomes challenging and (3) a means to correct for known hydrological effects in GNSS time series extensively used in tectonic studies. Indeed, GNSS provides insight into the 3D surface deformation field complementary to InSAR, particularly when it comes to horizontal displacements. This is important because, as we emphasize in this work, horizontal and vertical deformation fields arising from different mechanisms can have distinct spatial signatures.

Previous studies have described poroelastic deformation fields using a number of modeling frameworks, including the USGS modular finite-difference groundwater flow model (MODFLOW) (Hoffmann & Wilson, 2003), finite strain cuboids in a homogeneous elastic half-space (Barbot et al., 2017; Silverii et al., 2019; Hu & Bürgmann, 2020) and

mixed finite element models (Ferronato et al., 2010; Alghamdi et al., 2020). In this work, we present an alternative framework to characterize the vertical and horizontal surface displacements arising from poroelastic eigenstrains in an unconfined aquifer with heterogeneous elastic properties (Fleitout & Chanard, 2018). We hope that the resulting (semi-)analytical solutions can serve as an intermediate between models with homogeneous elastic properties and more involved numerical models, and hence provide further insight into the complex, three-dimensional deformation field of aquifer systems.

The manuscript is organized as follows: We first introduce the geohydrological setting and data sets of our study area in Section 2. We selected the Ozark Plateaus Aquifer System (OPAS) in central United States to test the method because of the relatively quiescent tectonic setting (Craig & Calais, 2014; Calais et al., 2016), the data availability and the well-documented geohydrological setting (e.g., Imes & Emmett, 1994; Hays et al., 2016; Westerman et al., 2016; Knierim et al., 2017). In Section 3, we characterize the heterogeneous groundwater level dataset with an Independent Component Analysis (ICA). We then present analytical solutions for simple disk loading and aquifer scenarios before extracting the 3D poroelastic deformation field from the GNSS time series in Section 4. We conclude the study by inferring the heterogeneous distribution of elastic moduli in OPAS from the extracted groundwater level variations and vertical poroelastic displacements in Section 5.

2 Regional setting and data sets

2.1 The Ozark Plateaus Aquifer System (OPAS)

OPAS is a large system of aquifers and confining units in the Mississippi River basin in central United States (Figure 2). The system is bounded by the Mississippi River and its alluvial plain, the Missouri River and Arkansas River to the east, north and south, respectively, and by a saline to freshwater transition zone to the west (Imes & Emmett, 1994) (Figure 2A). Although it is a significant source of water for agricultural and public supply in the region, groundwater use in OPAS represents a relatively small portion of the hydrologic budget – about 2% of aquifer recharge (Hays et al., 2016). Most groundwater recharge flows laterally, feeding other aquifers and sustaining streams, lakes and wetlands (Hays et al., 2016). Nonetheless, groundwater pumping does cause localized cones of depression around certain urban areas such as Springfield, Missouri (Imes, 1989).

OPAS is composed of interbedded layers of carbonate and clastic deposits around the topographic high Ozark dome (Hays et al., 2016; Westerman et al., 2016). The system is underlaid by a basement confining unit which outcrops at the Ozark dome in east-central Missouri (Figure 2AC). The Ozark aquifer system (OAS) – the most important water-bearing unit of the system – crops out at the center of the system and is otherwise overlaid by the Springfield Plateau aquifer system (SPAS) and/or the Western Interior Plains confining system (WIPCS). North of the Missouri - Arkansas border, carbonate-rich units such as SPAS and OAS present rich karst features (Hays et al., 2016).

Other aquifer systems surrounding OPAS are also shown in Figure 2. The Mississippi Embayment Aquifer System and the shallower Mississippi River Valley Aquifer southeast of OPAS supply much of the irrigation water for the agriculture-intensive region (Hart et al., 2008). The Mississippian Aquifers and glacial deposits from the Laurentide Ice Sheet occupy the north and northeastern boundaries of the study area (Bayless et al., 2017).

2.2 Data sets

2.2.1 Groundwater level time series

Groundwater monitoring wells (i.e., piezometers) record the temporal evolution of hydraulic head at a given depth. In this study, we take advantage of the piezometric network maintained by the United States Geological Survey which provides daily observations of water level depth (USGS Water Services; https://waterservices.usgs.gov). Of the 312 wells in the study area, we retain the 167 sites with 60% or more data completeness during the 2007 to 2017 timespan and further exclude seven stations classified as anomalous after visual inspection (Figure S1). For example, two time series with a typical groundwater pumping signature (Figure S1) are excluded from the analysis because these signals are expected to be very local (tens of meters) - as they represent the aquifer response to local forcings - and to bias the analysis due to their large amplitudes. We subtract the altitude at each well location to obtain the hydraulic head, detrend the time series and compute monthly averages to facilitate comparison with the other data sets used in this study. The positions of the 160 selected wells are shown in Figure 3A and examples of retained time series are presented in Figure 3B. They present seasonal and multiannual water level oscillations from a few to tens of meters in amplitude.

2.2.2 GRACE-derived displacement time series

GRACE satellites monitor space and time variations in Earth's gravity field from which changes in continental water storage - which include both surface and groundwater mass (Figure 1A) - can be inferred and expressed in units of equivalent water height (EWH). At the global scale, GRACE-based models have been shown to better explain the seasonal signals in GNSS datasets than hydrology-based models (Li et al., 2016). Here, we make use of the Level 2 Release 06 spherical harmonics GRACE solution up to degree 96 where low degree harmonics C_{20} have been replaced by SLR-derived values provided by the Center for Space Research (CSR) (Bettadpur, 2018; GRACE, 2018) and DDK5-filtered to minimize north-south striping noise (Kusche et al., 2009). We add back the atmospheric and non-tidal oceanic contributions as these effects are not corrected in the GNSS data set and detrend the resulting time series. The colormap in Figure 3A shows the average annual EWH peak-to-peak amplitudes observed during the 2007 to 2017 timespan and reveals an important large-scale NW to SE gradient in regional water storage changes, with higher amplitudes concentrated around the Mississippi Alluvial Valley.

To quantify the large-scale hydrological elastic loading deformation resulting from changes in surface water and groundwater mass (Figure 1B), we compute the deformation expected from GRACE-inferred loads at the GNSS sites using a spherical elastic layered Earth model based on the Love number formalism (Farrell, 1972; Chanard et al., 2018).Note that while hydrological loading can, in theory, produce both elastic and viscoelastic deformation fields, here we limit our analysis to a purely elastic model given that the Earth's response is in phase with loading at the annual and multiannual timescales. Moreover, while changes in groundwater mass do not occur exactly at the surface of the Earth, the depth at which those changes occur (on the order of 1 km at most) is negligible compared to the radius of the Earth, which is the key quantity in elastic loading equations on a spherical Earth (Farrell, 1972). For example, using a radius of 6370 km instead of 6371 km would result in a 0.01% change in the computed surface displacements. We therefore neglect this depth dependency in our calculations. Given the relatively large spatial wavelengths considered here, we also neglect the effect of relatively weak aquifer layers. Examples of the resulting time series are compared to the corresponding GNSS measurements in Figure S2. In Figure S3, we show that the modeled displacements in this region are relatively insensitive to the particular choice of GRACE solution as solutions from the CSR, JPL and GFZ centers all produce displacements with

mean absolute differences smaller than 1 mm (the approximate uncertainty of GNSS measurements).

2.2.3 GNSS displacement time series

GNSS tracks the vertical and horizontal displacements of geodetic monuments anchored a few meters below the ground surface (or on top of buildings for fewer than 15% of stations). In this analysis, we start from the time series processed by the Nevada Geodetic Laboratory and expressed in the IGS14 reference frame (International GNSS Service), based on the latest release of the International Terrestrial Reference Frame (ITRF2014), (Altamimi et al., 2016; Blewitt et al., 2018, http://geodesy.unr.edu). Of the 315 stations located in the study area which is delimited by longitudes -96^{o} to -89^{o} and latitudes 34.5^{o} to 40.5^{o}, we retain the 92 stations with at least 60% of daily data between 2007 and 2017. After visual inspection, six additional stations (CVMS, MOGF, MOMK, MOSI, NWCC, and SAL5) are discarded due to spurious large amplitude signals. The positions of the remaining 86 stations are shown in Figures 3A and S4.

For each time series, we fit a trajectory model (Bevis & Brown, 2014) with a linear trend, annual and semi-annual terms and step functions to account for material changes and potential coseismic displacements (http://geodesy.unr.edu/NGLStationPages/steps.txt) as well as visually obvious offsets. We subtract the best-fit linear trend and step functions from the time series but do not correct for the periodic terms. Next, we identify and eliminate outliers defined as points that exceed three times the average deviation from the 90-day median for any of the three directions (east, north, vertical). The time series are then monthly averaged to match the GRACE temporal resolution. Finally, the spherical harmonic degree-1 deformation field is estimated from a global network of 1150 GNSS stations and subtracted from retained GNSS time series to allow for a direct comparison with GRACE observations which do not capture degree-1 mass changes (Chanard et al., 2018). Examples of the resulting time series are provided in Figure S2.

3 Fluctuations in groundwater levels

The first step towards extracting poroelastic signals from our GNSS dataset is to characterize the groundwater fluctuations responsible for the deformation. This requires some form of spatial interpolation since piezometers only probe groundwater levels at discrete points in space and are generally not co-located with GNSS stations. We determine that directly interpolating between the piezometric sensors is not warranted in this case given the heterogeneous nature of aquifers and the variable depth of wells (Figure 3). For example, neighboring piezometers GW1 and GW2 in Figure 3B reveal very different temporal signatures. On the other hand, GW2 and GW3 - which are over 200 km apart - have highly correlated time series. Groundwater fluctuations at GW4 also correlate with GW2 and GW3 but are of much higher amplitude. The groundwater dataset thus contains both regional- and local-scale signals with peak-to-peak amplitudes that span two orders of magnitude ($\sim$0.5 to 50 m).

3.1 Extracting groundwater signals with ICA

In light of these observations, we perform an Independent Component Analysis (ICA) on the groundwater dataset to extract the main modes of variability before proceeding with the spatial interpolation. ICA algorithms seek to recover the statistically independent sources of signal assumed to generate the linearly mixed time series at each sensor (Roberts & Everson, 2001). In particular, variational Bayesian ICA (vbICA) (Choudrey, 2002) has been shown to perform well to recover geophysical signals (e.g., postseismic, hydrology-induced and common mode error) from synthetic and real GNSS data sets (Gualandi et al., 2016; Larochelle et al., 2018). Once an independent component (IC) - i.e.

a source of signal - i is isolated, it can be expressed with space and time vectors as $\mathrm{IC}_i = U_i S_i V_i^T$ where U_i is a normalized spatial distribution, S_i is a weighting factor and V_i is a normalized temporal function.

Figure 4 shows the temporal functions (A), weighting factors (A) and spatial distributions (B-D) obtained from a 3 components vbICA of the groundwater dataset. We use a triangulation-based natural neighbor algorithm (MATLAB, 2017) to interpolate the spatial distributions from the discrete data points (Figure 4B-D). We choose to limit our analysis to 3 components since analyses with more components (e.g., see Figure S5 for a 5 components analysis) yield similar IC1-3 and additional lower-amplitude ICs with spurious temporal functions that only explain a limited portion of data variance. The retained temporal functions all display a mix of multiannual and seasonal frequencies.

IC_1, the component which explains the greatest share of data variance, has an overall positive spatial distribution and is observed at almost all wells including those outside OPAS (Figure 4B). This spatial distribution is indicative of a regional income of water linked to recharge processes (Longuevergne et al., 2007). The large fluctuations occurring in southern Missouri (e.g., at station GW4 (Figure 3)) are likely linked to the high storage capacity of thick limestone layers with limited karstification (Figure 4B). Figure S6 also reveals a crude spatial correlation between sinkhole density, which suggests a higher ability to recharge the aquifer system, and wells with high S_1U_1 values. IC_2 and IC_3 represent seasonal and multi-annual signals with different phases than IC_1 and exhibit heterogeneous spatial distributions with positive and negative values (Figure 4CD). These components probably compensate for local deviations from the regional behavior due to the delayed response of deeper aquifers, differing recharge and discharge mechanisms and groundwater pumping.

3.2 Comparing regional-scale hydrological signals across datasets

Given that IC_1 spans the entire study region, we expect to find a similar signal in the GRACE dataset. Performing a vbICA on the GRACE-predicted vertical displacements - completely independently from the groundwater ICA - the temporal function of the first and most important component indeed correlates very well with V_1^{GW}, as evidenced by the correlation coefficient ρ of -0.81 (Figure 5A). Downward motion occurs concurrently with rising groundwater levels because GRACE-derived vertical displacements solely reflect the hydrological loading deformation due to changes in continental water storage (Figure 1B), not the poroelastic deformation (Figure 1C). The associated spatial response (Figure 5B) reflects the northwest to southeast gradient of hydrological loads.

By contrast, GNSS vertical time series should comprise both deformation fields. Performing a similar analysis on the GNSS dataset independently from the groundwater and GRACE analyses results in a lower but still significant correlation of $\rho = -0.52$ with V_1^{GW} (Figure 5A). Note that a significant portion of GNSS stations sitting on top of OPAS were not installed until 2010 or 2011 as indicated by the grey shading in Figure 5A. Although the GNSS spatial distribution displays the same overall gradient as the GRACE-derived model with generally higher amplitudes around the Mississippi Alluvial Valley, the response is more heterogeneous (Figure 5B).

This comparison exercise demonstrates that the dominant temporal functions of all three datasets are in phase on a monthly timescale. This is consistent with a relatively uniform regional recharge of the aquifer system (Figure 4B) and with the system's karstic nature which allows for rapid communication between surface water and groundwater (Hays et al., 2016), suggesting that the aquifer's global behavior can be considered as unconfined. We recognize that OPAS is a complex aquifer system with both confined and unconfined units (Figure 3A) and that different hydrogeologic processes might interact to generate surface displacements. However, in this work, we choose to treat OPAS

as an effectively unconfined system and infer mechanical properties under this assumption.

4 Poroelastic deformation

4.1 Hydrological elastic loading vs poroelastic eigenstrain: Insights about surface displacements from simple analytical solutions

To gain intuition about the elastic and poroelastic deformation fields we expect to find in the vicinity of an unconfined aquifer, we first develop and compare analytical solutions for surface displacements associated with the simple disk scenarios shown in Figure 1BC, assuming an elastic half-space medium. In Appendix A, we extend the poroelastic solution to an arbitrary 2D eigenstrain distribution which we later use to predict horizontal poroelastic displacements. While we rely on this elastic half-space model with an aquifer layer to analyse and model poroelastic displacements in later sections, we only show the equivalent elastic half-space loading model in this section for illustration and comparison purposes.

4.1.1 Disk loading of an elastic half-space

We first consider a disk load of radius a and uniform pressure P at the surface of an elastic half-space with Young's modulus E_{deep}, representative of hydrological loading from surface water (Figure 1B). The corresponding vertical and horizontal surface displacements were derived by Johnson (1987) and Verruijt (2009) as:

$$u_z(r) = \begin{cases} -\dfrac{4(1-\nu^2)}{\pi E_{deep}} Pa\mathcal{E}\left(\dfrac{r^2}{a^2}\right), & r \le a \\ -\dfrac{4(1-\nu^2)}{\pi E_{deep}} Pr\left(\mathcal{E}\left(\dfrac{a^2}{r^2}\right) - \left(1-\dfrac{a^2}{r^2}\right)\mathcal{K}\left(\dfrac{a^2}{r^2}\right)\right), & r > a \end{cases} \quad (1)$$

$$u_r(r) = \begin{cases} -\dfrac{(1-2\nu)(1+\nu)}{2E_{deep}} Pr, & r \le a \\ -\dfrac{(1-2\nu)(1+\nu)}{2E_{deep}} P\dfrac{a^2}{r}, & r > a \end{cases} \quad (2)$$

where $u_z(r)$ and $u_r(r)$ are the vertical and horizontal displacements as a function of radial distance r and $\mathcal{K}$ and $\mathcal{E}$ are the complete elliptic integral of the first and second kind, respectively.

Figure 6A shows the deformation resulting from 10 km and 25 km-radius disks uniformly loaded with 5 m of water. Both the vertical and horizontal displacements extend beyond the loaded region with the maximum vertical and horizontal displacements occurring at the center of the disk and at the load boundary, respectively. Note that the amplitude of deformation is proportional to the spatial wavelength of the load.

4.1.2 Poroelastic eigenstrain in a disk within an elastic half-space

Poroelastic deformation arises from dilational eigenstrains (Mura, 1982) associated with changes in pore pressure, analogous to thermoelastic deformation resulting from changes in temperature. In fact, the solutions derived here are directly applicable to the equivalent thermoelastic problem (Fleitout & Chanard, 2018). Eigenstrains refer to internal strains which, in the absence of external stresses resisting them, would lead to isotropic expansion or contraction of the body. In the poroelastic case, eigenstrains are related to changes in pore pressure, Δp, and hence in groundwater level, Δh, as:

$$\varepsilon_{eig} = \frac{\beta \Delta p(1-2\nu)}{E_{aq}} = \frac{\beta \rho g \Delta h(1-2\nu)}{E_{aq}} \quad (3)$$

where β, ν and E_{aq} are the Biot-Willis coefficient, Poisson's ratio and Young's modulus of the aquifer layers, respectively, while ρ is water density and g is the gravitational acceleration.

Given the relatively high hydraulic conductivity of karstified sedimentary rocks (Domenico & Schwartz, 1998; Hays et al., 2016), in this work we assume that there is no significant time delay between changes in pore pressure and the resulting deformation. We also assume that deformation is entirely (poro)elastic and neglect permanent deformation as clay minerals often responsible for inelastic processes are seldom found in OPAS (Westerman et al., 2016).

Linear elastic constitutive equations accounting for eigenstrains are as follows (Wang, 2000):

$$\varepsilon_{zz} = \frac{1}{E_{aq}}\left[(1+\nu)\sigma_{zz} - \nu(\sigma_{rr}+\sigma_{\theta\theta}+\sigma_{zz})\right] + \varepsilon_{eig} \tag{4}$$

$$\varepsilon_{rr} = \frac{1}{E_{aq}}\left[(1+\nu)\sigma_{rr} - \nu(\sigma_{rr}+\sigma_{\theta\theta}+\sigma_{zz})\right] + \varepsilon_{eig} \tag{5}$$

$$\varepsilon_{\theta\theta} = \frac{1}{E_{aq}}\left[(1+\nu)\sigma_{\theta\theta} - \nu(\sigma_{rr}+\sigma_{\theta\theta}+\sigma_{zz})\right] + \varepsilon_{eig} \tag{6}$$

Given that lateral motion is restrained by the elastic medium below, it can be shown that horizontal strains within the aquifer layers, ε_{rr} and $\varepsilon_{\theta\theta}$, although not strictly null, are negligible compared to ε_{eig} in this case (Fleitout & Chanard, 2018). Under this assumption, lateral stresses, σ_{rr} and $\sigma_{\theta\theta}$, can be approximated as:

$$\sigma_{rr} = \sigma_{\theta\theta} = \frac{-E_{aq}\varepsilon_{eig} + \nu\sigma_{zz}}{1-\nu} \tag{7}$$

where σ_{zz} is the change in total vertical stress associated with a change in groundwater level Δh:

$$\sigma_{zz} = -\phi\rho g\Delta h \tag{8}$$

where ϕ is the porosity of the aquifer layers and the negative sign indicates compressive stresses. Substituting Equations (3), (7) and (8) into (4) and integrating the vertical strain over the saturated aquifer thickness b and radius a yields the following vertical deformation field at the surface:

$$u_{z,exp}(r) = \begin{cases} \dfrac{(1+\nu)(1-2\nu)}{(1-\nu)}\dfrac{(\beta-\phi)\rho g\Delta h(r) b}{E_{aq}}, & r \le a \\ 0, & r > a \end{cases} \tag{9}$$

Here we must integrate over the entire saturated thickness b since pore pressure increases over the entire depth of the hydraulically-connected aquifer when it is recharged with additional water. Equation (9) describes the vertical poroelastic expansion of the aquifer layers in excess of the elastic loading deformation resulting from the added groundwater load ($\phi\rho g\Delta h$) within these elastically weak layers.

The total horizontal strain, sum of the elastic and eigenstrain, has to be small compared to the eigenstrain because it requires deformation of the elastic medium below the aquifer. In fact, compensation of horizontal eigenstrain by elastic strain requires strong variations in lateral stress σ_{rr} within the aquifer (Equation (7)). These variations in σ_{rr} necessarily induce shear stresses at the base of the aquifer, which results in both horizontal and vertical displacements within the medium below the aquifer. We can see this effect by solving for this basal shear stress, $\sigma_{rz}(z=b)$, considering the stress equilibrium equations for an axisymmetric problem in cylindrical coordinates:

(Wang, 2000):

$$\frac{\partial\sigma_{rz}}{\partial r} + \frac{\partial\sigma_{zz}}{\partial z} + \frac{\sigma_{rz}}{r} = 0 \tag{10}$$

$$\frac{\partial \sigma_{rz}}{\partial z} + \frac{\partial \sigma_{rr}}{\partial r} + \frac{\sigma_{rr} - \sigma_{\theta\theta}}{r} = 0 \tag{11}$$

Substituting Equation (7) into (11), integrating with respect to z and applying a zero shear stress boundary condition at the surface ($\sigma_{rz}(z = 0) = 0$) yields:

$$\sigma_{rz}(z = b) = -\int_0^b \frac{\partial}{\partial r}\left[\frac{-E_{aq}\varepsilon_{eig} + \nu\sigma_{zz}}{1-\nu}\right]\partial z \tag{12}$$

$$= \frac{\partial}{\partial r} I(r) \tag{13}$$

where

$$I(r) = \int_0^b \frac{E_{aq}\varepsilon_{eig} - \nu\sigma_{zz}}{1-\nu}\partial z \tag{14}$$

is the fundamental quantity driving poroelastic deformation (Fleitout & Chanard, 2018). For the simple disk aquifer considered here, E_{aq}, ε_{eig}, ν and σ_{zz} are uniform within the aquifer and ε_{eig} and σ_{zz} are equal to zero outside the aquifer such that:

$$I(r) = \frac{(E_{aq}\varepsilon_{eig} - \nu\sigma_{zz})b}{1-\nu}\mathcal{H}(a - r) \tag{15}$$

$$= \frac{(\beta(1-2\nu) + \phi\nu)\rho g \Delta h b}{(1-\nu)}\mathcal{H}(a - r) \tag{16}$$

$$= I_{disk}\mathcal{H}(a - r) \tag{17}$$

and

$$\sigma_{rz}(z = b) = I_{disk}\delta(r - a) \tag{18}$$

where $\mathcal{H}$ and δ are the Heaviside and Dirac delta functions, respectively. Finally, we predict the deformation induced by $\sigma_{rz}(z = b)$ with the expressions derived by Johnson (1987) for surface displacements due to an axisymmetric shear stress distribution, $q(t)$:

$$u_{z,shear}(r) = \begin{cases} -\dfrac{(1-2\nu)(1+\nu)}{\pi E_{deep}}\displaystyle\int_r^a q(t)dt, & r \le a \\ 0, & r > a \end{cases} \tag{19}$$

$$u_{r,shear}(r) = \frac{4(1-\nu^2)}{\pi E_{deep}}\int_0^a \frac{t}{t+r} q(t)\left[\left(\frac{2}{k^2} - 1\right)\mathcal{K}(k) - \frac{2}{k^2}\mathcal{E}(k)\right]dt \tag{20}$$

where $k^2 = 4tr/(t + r)^2$. Using $\sigma_{rz}(z = b)$ as $q(t)$, inclusive limits of integration and the sifting property of the Dirac delta function results in:

$$u_{z,shear}(r) = \begin{cases} -\dfrac{(1-2\nu)(1+\nu)}{\pi E_{deep}} I_{disk}, & r \le a \\ 0, & r > a \end{cases} \tag{21}$$

$$u_{r,shear}(r) = \frac{4(1-\nu^2)}{\pi E_{deep}} I_{disk}\frac{a}{a+r}\left[\left(\frac{2}{k^2} - 1\right)\mathcal{K}(k) - \frac{2}{k^2}\mathcal{E}(k)\right] \tag{22}$$

where $k^2 = 4ar/(a + r)^2$. At $r = a$, $u_{r,shear}$ has an infinite value. Our mathematical framework is derived in a "thin layer" approximation, and therefore only valid for spatial wavelengths larger than the aquifer thickness. It would be possible to derive analytical solutions in a more complex mathematical framework for shorter wavelengths. However, for simplicity, we choose to numerically approach the diverging solution of Equation (22) at $r = a$ by truncating its expansion series (Appendix B), which has no impact at distances larger than the aquifer thickness.

To obtain an order of magnitude estimate of the poroelastic displacements expected in OPAS, we compute the poroelastic deformation generated by a 20 m increase in groundwater level in unconfined disk aquifers with radii of 10 km and 25 km and a thickness of 1000 m (Figure 6B). These parameter values are representative of the localized zone of elevated groundwater variations observed at the center of OPAS (Figure 4B) and are consistent with the equivalent elastic loading scenarios shown in Figure 6A, assuming a porosity of 25%. The vertical displacement is largely due to poroelastic expansion and is bounded by the aquifer. The horizontal poroelastic displacement, on the other hand, is entirely due to the shear stress imposed at the base of the aquifer and extends beyond the aquifer. Moreover, the amplitude of deformation is independent of the wavelength of pore pressure perturbation in contrast to the hydrological loading case. Indeed, the 10 and 25 km disks result in displacements of the same amplitude.In fact, expressions for horizontal displacements given by Equations (2) and (22) become independent of the disk radius a when evaluated for distances $r = r/a$. We rely on the observation that poroelastic displacements only depend on local changes in pore pressure to justify the use of elastic half-space models - as opposed to a spherical Earth model - for the upcoming analysis.

4.2 Extraction of geodetic poroelastic displacements

In order to extract poroelastic deformation from GNSS time series, we first assume that deformation from hydrological loading is well reproduced by the GRACE model and hence focus on the GNSS - GRACE residual time series. This assumption is supported by a comparison of the vertical time series in Figures 7 and S2. The geodetic deformation at station ZKC1 located outside OPAS and other aquifer systems (Figure 3A) is well explained by the GRACE model and presents very little residual seasonal displacements (Figure 7A). This is consistent with Chanard et al. (2018)'s finding that vertical displacements observed by GNSS are generally well explained by a GRACE loading model at a global scale because most stations are located at bedrock sites. At station MOWS at the center of OPAS, on the other hand, the GNSS vertical displacements deviate from that predicted from loading effects and the residuals show clear seasonal and multiannual features (Figure 7B).

For the horizontal components, we first estimate and remove the common mode deformation from the GNSS-GRACE residual time series to isolate OPAS's poroelastic response. We estimate the common mode by taking a spatial average of all horizontal GNSS-GRACE residual time series within the study area. This step is necessary as Figure S7 illustrates that neighbouring aquifers can induce significant horizontal poroelastic deformation within the study region. Although the horizontal displacements in OPAS caused by the synthetic poroelastic eigenstrains in Figure S7D are affected by boundary effects and vary with distance from the perturbed zone, most stations do move in the same direction, similar to the displacements extracted through our methodology but without removing the common mode (Figure S7C). Subtracting the common mode from GNSS-GRACE residual time series should thus account for the first order effects of neighbouring aquifers.

We posit that at least part of these seasonal and multiannual residuals can be attributed to instantaneous poroelastic deformation and should therefore be proportional to and in phase with groundwater fluctuations. Since we know the dominant temporal functions that make up the groundwater fluctuations, we can test this hypothesis by projecting the residual geodetic time series onto these functions. However, unlike the related Principal Component Analysis (PCA) technique, ICA yields independent components which are not constrained to be orthogonal. Before proceeding with the projection, we must thus orthogonalize vectors V_1^{GW}, V_2^{GW} and V_3^{GW} from Section 3.1 via the Gram-Schmidt process to produce an orthogonal basis, enabling us to sum the contribution of

each basis vector as follows:

$$P_j = \frac{R_j \cdot W_1}{\|W_1\|^2} W_1 + \frac{R_j \cdot W_2}{\|W_2\|^2} W_2 + \frac{R_j \cdot W_3}{\|W_3\|^2} W_3 \tag{23}$$

where P_j is the inferred poroelastic displacement for direction j (i.e., east, north or up), R_j is the GNSS-GRACE residual time series and W_1, W_2, W_3 are the orthogonalized versions of $V_1^{GW}, V_2^{GW}, V_3^{GW}$. Figure S8 reveals that the V_i^{GW}'s were not far from orthogonality to start with since W_2 and W_3 only differ marginally from V_2^{GW} and V_3^{GW}, respectively.

The resulting P_j's are shown in yellow in Figure 7 and Figure S2. The recovered vertical poroelastic deformation is relatively small at station ZKC1 outside of aquifer systems and relatively large at station MOWS at the center of OPAS. However, both stations exhibit similar amplitudes of horizontal poroelastic deformation. This behavior is consistent with the analytical solutions developed in Section 4.1.

4.3 Vertical poroelastic displacements

Figure 8 illustrates the amplitudes of the poroelastic signals extracted with each groundwater temporal function W_i. Similar to the groundwater spatial distributions in Figure 4, the vertical poroelastic signal recovered with W_1 is mostly positive and is more extensive and of higher amplitude than the signals recovered with W_2 and W_3. The poroelastic signals associated with W_2 and W_3 present both positive and negative values like the S_2U_2 and S_3U_3 distributions of groundwater.

Focusing on this regional signal, Figure 8A shows that many stations outside OPAS exhibit amplitudes comparable to those inside OPAS. We attribute these poroelastic displacements to the other major aquifer systems present in the region (Figure 2). Westernmost stations (e.g., ZKC1) where major aquifer structures are sparse or non-existent display some of the smallest amplitudes. However, it is difficult to evaluate whether or not a GNSS station is sitting on top of an aquifer system since the map in Figures 2 and S4 only indicates the surface outcrops of these aquifer systems. The particularly large seasonal displacements at station OKMU (Figure S2C) at the southwestern edge of OPAS might be due to intensive groundwater pumping. Unfortunately there is no nearby groundwater monitoring well active during this time period to test this hypothesis. Finally, as Eq. (9) suggests, the range of vertical poroelastic amplitudes observed within OPAS - from about 2 to 14 mm - may reflect differences in poroelastic (β, ϕ, E_{aq}) properties, groundwater variations (Δh) or saturated aquifer thickness (b). We discuss this further in Section 5.

4.4 Horizontal poroelastic displacements

As for horizontal displacements, Figure 8D-F suggests that all three temporal functions W_i's are associated with spatially heterogeneous poroelastic deformation on the order of a few millimeters. According to Equation (22), poroelastic horizontal displacements are governed by deep elastic parameters as opposed to the aquifer properties relevant for vertical poroelastic expansion. Elastic properties are believed to be more laterally homogeneous at depth than at the surface. Indeed, as discussed in Section 5.2, surficial layers are more prone to fracturing which can alter elastic moduli. We thus approximate E_{deep} with a constant value of 80 GPa and use Equations (A3) and (A4) for a spatially variable 2D distribution $I(x, y)$ (A1) to predict the horizontal poroelastic deformation induced by the observed groundwater fluctuations.

The colormaps in Figure 8D-F show the spatial distributions of $I(x, y)$ interpolated within OPAS for each groundwater IC as well as the resulting displacements at the GNSS sites (red arrows). Although the model predictions associated with W_1 match the observed displacements to first order at a handful of stations within OPAS, the observa-

tions are more heterogeneous than predicted (Figure 8D). For example, station MOBW undergoes a 7 mm displacement to the southwest whereas the model predicts a sub-millimetric eastward displacement (Figure S2D). The models for W_2 and W_3, on the other hand, fail to match the extracted displacements (Figure 8EF).

There are a number of potential reasons for these discrepancies. First and foremost, horizontal poroelastic displacements are highly sensitive to local variations in groundwater levels since they depend on the gradient of the groundwater field (e.g., Equation (13)) and do not attenuate with decreasingly small perturbation wavelengths. Hence, the spatial resolution of the piezometric network might be insufficient to accurately model the horizontal deformation. One way to improve the analysis would be to refine the spatial resolution of surface deformation measurements using InSAR (with the caveat that InSAR is mostly sensitive to east-west and vertical deformation). The model could also be extended to account for perturbation wavelengths smaller than the thickness of the aquifer. Some of the large horizontal displacements might also be due to hydrogeologic phenomena not included in the present model. For example, Silverii et al. (2016) and Serpelloni et al. (2018) explain horizontal transient signals observed around karstic aquifers with the opening and closing of vertical tensile dislocations due to groundwater variations. Groundwater pumping and the associated cones of depression might also be inducing horizontal deformation within the aquifer system itself (Helm, 1994).

Finally, our projection methodology might be capturing sources of seasonal and multi-annual signals not associated with groundwater. In particular, Fleitout & Chanard (2018) show that important horizontal thermoelastic displacements can result from sharp variations in elastic properties. Heterogeneities in hydrological loading from surface water not captured by GRACE might also be responsible for some of the discrepancy. However, this would require relatively strong heterogeneities in surface water variations since, as demonstrated in Figure 6A and as opposed to poroelastic deformation, the amplitude of deformation associated with hydrological elastic loading decreases with decreasing load size. In the next section, we present a preliminary analysis to quantify the displacements induced by surface hydrological fluctuations not detected by GRACE.

4.5 Hydrological loading from small-scale surface water heterogeneities

As the GRACE model only captures long-wavelength hydrological loads, our GNSS-GRACE residuals may contain signals from small-scale hydrological surface loads in addition to groundwater-related deformation. Thoroughly quantifying the role of these small-scale heterogeneities in GNSS time series would require a sufficiently resolved spatiotemporal characterization of surface water variations throughout OPAS. We can, however, assess how important this effect is in our study area by considering the illustrative case of the Harry S. Truman Reservoir in central Missouri for which we have a record of the water levels (`https://waterdata.usgs.gov/nwis/dv?referred_module=sw&site_no=06922440`) (Figure 9AB). If fluctuations in the lake reservoir were causing important solid Earth deformation, we would expect that projecting GNSS-GRACE residuals of nearby stations onto the water level time series would result in significant projection signals, similar to the poroelastic case. In the case of vertical displacements, we would also expect the recovered signal to be in phase opposition with the water levels given the elastic loading nature of the deformation.

However, Figure 9CD reveals that performing such a projection at nearby stations MOCL and MOWW results in vertical signals of relatively small amplitudes and in phase with water levels. As for the horizontals, we do find a significant signal in the north component of station MOWW. The fact that the recovered signal is in phase with the groundwater projection suggests that the residuals could be due to elastic loading from the reservoir, poroelastic effects or a mix of both.

We can also use the analytical model from Section 4.1.1 to compute the elastic loading displacements expected from water level variations in the Truman Reservoir. In Figure 9E, we show that the displacements expected from a 5 m increase in water level over a circular region of radius 1.5 km - representative of the small portion of the Truman Reservoir closest to station MOCL - are below the 1 mm threshold of GNSS accuracy. Using a circular region with the same total surface area as that of the reservoir, on the other hand, does result in significant millimetric displacements at both stations MOWW and MOCL (Figure 9F). If the north displacements at station MOWW were indeed caused by elastic loading from the Truman reservoir, Figure 9F suggests that we should observe even larger displacements in the vertical direction. Since this is not what we observe in Figure 9D, we conclude that elastic loading from the Truman reservoir must be relatively small compared to the poroelastic effect. Although this analysis is limited to a single reservoir due to the paucity of water level data, we assume these findings to be representative of other lakes and reservoirs in the study area.

5 Aquifer mechanical properties

5.1 Estimating aquifer elastic parameters from vertical geodetic measurements

As discussed in Section 4, vertical poroelastic displacement is primarily due to the expansion and contraction of aquifer layers in response to groundwater fluctuations. Assuming that the system is effectively unconfined and that the ICs extracted in Section 3 indeed capture the groundwater variations responsible for the poroelastic deformation, we can estimate an effective aquifer Young modulus E_{aq} directly below each GNSS station by rearranging Eq. (9) as:

$$E_{aq} = \frac{(1+\nu)(1-2\nu)}{(1-\nu)} \frac{(\beta-\phi)\rho g \Delta h b}{u_{z,exp}} \tag{24}$$

To this end, we compare the interpolated groundwater fluctuations from Section 3 to the inferred vertical poroelastic deformation from Section 4. Note that E_{aq} only depends on the vertical displacement in Eq. (24) and, as such, poroelastic horizontal displacements are not used in constraining the elastic modulus. For each GNSS station where both datasets are available, we consider the slope and coefficient of determination, R^2, of the best-fit line through the displacement vs groundwater level space (Figure S9). The slope represents the ratio of vertical displacement to groundwater variation, $u_{z,exp}/\Delta h$, whose inverse enters Eq. (24) and R^2 quantifies the fit of the linear regression. The higher R^2 is, the more correlated the two datasets are and, hence, the more confident we are in the E_{aq} estimate. Figure 10A shows examples of vertical displacement and groundwater level time series with different R^2 values and Figure 10B illustrates the spatial distribution of R^2. We only retain stations with $R^2 > 0.35$ such as MOC3, ARBT and MOSD to estimate E_{aq}. Station ARHR illustrates a case where the time series are too incoherent to infer a meaningful value of E_{aq}. Stations with low R^2 might reflect localities where spatial interpolation of the groundwater ICs fails to reproduce the actual variations in groundwater levels. For example, station ARHR and two of its neighbours which also display low R^2 values are all located in a region with relatively few piezometric measurements.

For the thickness b, we assume that there is significant hydraulic connectivity between the different aquifer units making up OPAS (as evidenced by the temporal correlation in Figure 5A) and sum their thicknesses. We also assume that the aquifer is saturated over its entire thickness. Figure 10C shows the total thickness, b_{model}, derived from Westerman et al. (2016)'s hydrogeological model. We extrapolate this thickness distribution for GNSS stations that are within 0.2°of the OPAS surface trace. Assuming representative constant values of $\nu = 0.25$, $\beta = 0.80$, and $\phi = 0.25$ (Domenico & Schwartz,

1998), we obtain estimates of E_{aq} at the 30 retained sites where all three datasets (Δh, b_{model} and $u_{z,exp}$) are available (Figure 10D). We also interpolate between stations given that the vertical poroelastic field is governed by the relatively homogeneous spatial distribution associated with W_1 (Figure 8A). Figure 11 reveals that this (preferred) distribution of E_{aq} mostly falls between 1 and 10 GPa. We discuss these values further in Section 5.2.

5.2 Explaining low field estimates of E_{aq}

In Section 5.1 we estimated a distribution for E_{aq} with values ranging from 0.04 to 18 GPa and a median of 1.58 GPa (Figure 11). These values are lower than the laboratory-constrained elastic moduli of the principal rocks found in OPAS: limestone, dolomite, sandstone and shale (Westerman et al., 2016). For example, Ge & Garven (1992) suggest values of 125, 68, 9 and 11 GPa for the Young modulus of Blair Dolomite, Maxville Limestone, Berea Sandstone and Chattanooga Shale, respectively (see Table S1), pointing to an average Young modulus of the order of 50 GPa.

Here we investigate whether this order of magnitude discrepancy could be due to uncertainties on the various parameters involved in estimating E_{aq}. We evaluate the uncertainty on parameter b at $\pm$ 36 m based on the root mean square errors reported by Westerman et al. (2016). For the poroelastic constants, Domenico & Schwartz (1998) states that the Poisson ratio ν falls within 0.25 and 0.33 for most rocks and that the porosity ϕ of limestone (including karst limestone), dolomite, sandstone and shale ranges from 0 to 0.40. As for the Biot-Willis coefficient β, we infer a range of 0.60 to 0.90 based on the reported values of 0.69, 0.76 and 0.95 for limestone, sandstone and mudstone, respectively (Domenico & Schwartz, 1998).

We then compute the minimum and maximum expected distributions of E_{aq} in Figure 11 by considering the parameter values within these uncertainty ranges that minimize and maximize the factor $(1+\nu)(1-2\nu)/(1-\nu)(\beta-\phi)b$ in Equation (24). The medians of the resulting distributions are 0.43 and 2.73 GPa, respectively. Since the maximum estimated values of E_{aq} are still generally an order of magnitude smaller than those observed in the laboratory, we argue that there is a robust discrepancy between elastic modulus measured at these different scales.

Lower-than-expected elastic modulus cannot be explained by the potential underestimation of hydrological loading displacements associated with small-scale heterogeneities in surface water discussed in Section 4.5. Indeed, if the loading deformation is underestimated by GRACE, the vertical poroelastic response would be underestimated as well and hence the Young modulus would be overestimated. This is because vertical poroelastic and elastic loading displacements act in opposite directions. For example, if the actual loading induces a -5 mm deformation and the poroelastic displacement is 10 mm, GNSS would record a net signal of 5 mm (since GNSS = poroelastic + loading). Now if GRACE underestimates the loading deformation at -3 mm instead of -5 mm, we would underestimate the poroelastic signal at 8 mm instead of 10 mm and, thus, overestimate the Young modulus.

There is, however, a growing body of evidence that laboratory-based values overpredict *in situ* estimates of effective elastic moduli (e.g., Matonti et al., 2015; Bailly et al., 2019). Matonti et al. (2015), for instance, report seismic velocities, V_p, measured on carbonate rock outcrops that are up to 70% smaller than those obtained on rock samples in the laboratory, implying a tenfold reduction in elastic moduli. Although part of the discrepancy is probably due to the greater porosity observed in the field (e.g., due to karstic features in this case), Fortin et al. (2007) and Bailly et al. (2019) have shown that seismic velocities - and hence elastic moduli - are more sensitive to geological features with high aspect ratios such as cracks, fractures, bedding plane and faults because they are more compliant to deformation than spherical pores.

Following the effective medium theory framework of Fortin et al. (2007), the ratio of effective bulk modulus K to bulk modulus of the intact rock, K_o, can be described in terms of porosity, ϕ, and fracture density, f, defined as $f = Nc^3/V$, where N is the number of penny-shaped cracks with radius c, embedded in a volume V (Walsh, 1965):

$$\frac{K_o}{K} = 1 + \frac{3}{2}\frac{(1-\nu_o)}{(1-2\nu_o)}\phi + \frac{16}{9}\frac{(1-\nu_o^2)}{(1-2\nu_o)}f \tag{25}$$

where ν_o is the Poisson ratio of the intact rock. Assuming $\nu_o = 0.25$, Eq. (25) reduces to:

$$\frac{K_o}{K} = 1 + 2.25\phi + 3.33f \tag{26}$$

Thus, a fourfold reduction in elastic modulus ($K_o/K = 4$) for example would require - assuming a spherical pore porosity of 25% - a fracture density f of 0.7, a common value reported in fractured reservoirs (Bailly et al., 2019). We thus conclude that the reduction in elastic moduli is mostly due to the presence of fracture-like geological features as in previous studies (Matonti et al., 2015; Bailly et al., 2019).

6 Conclusions

To summarize, in this study, we characterized the spatiotemporal variations of OPAS's groundwater levels with three independent components. In particular, we uncovered a regional-scale groundwater signal that is temporally correlated with geodetic observations. Then, by assuming that large-scale hydrological loading displacements are well described by a GRACE-based model and that poroelastic deformation is in phase with groundwater fluctuations, we extracted vertical and horizontal poroelastic displacement fields from GNSS time series by projecting onto the groundwater temporal functions. We also quantified the amplitudes of displacements induced by hydrological loading vs poroelastic effects with analytical solutions and developed a 2D poroelastic model to relate groundwater perturbations in an unconfined aquifer system to surface displacements. Finally, we found that the extracted groundwater variations and vertical poroelastic displacements imply an heterogeneous spatial distribution of Young modulus with values no larger than a few GPa's.

Our findings have important implications in the fields of hydrology, geodesy and seismology. First, the excellent correlation between the GRACE and groundwater temporal functions indicates that there is consistency between the water mass fluctuations observed at the local and continental scales. Filtering groundwater levels dataset with ICA could also lead to improved piezometric maps free of aberrant local signals. In terms of poroelastic displacements, the OPAS example clearly demonstrates that both hydrological loading and poroelastic effects can induce significant geodetic deformation in the vertical and horizontal directions - hence the need to account for both deformation fields when correcting GNSS time series for hydrological effects. Since the two types of deformation can interfere destructively, failing to account for poroelastic effects in hydrogeodetic inversions could result in large errors in estimates of total water storage variations. The notion that poroelastic stresses may be locally stronger than those generated from hydrological loading (due to their relative amplitudes at small perturbation wavelengths) also warrants revisiting the role of both sources of stress in triggering seasonal seismicity (Craig et al., 2017). Lastly, our relatively low geodetic estimates of Young modulus motivates further investigation into surficial elastic parameters and their effect on global hydrological loading models (Chanard et al., 2018).

While this study is clarifying the signature of large aquifer systems in GNSS time series, further work is certainly necessary to address the current limitations of our methodology, starting with testing the validity of the method in other aquifer settings. In par-

ticular, the methodology should be evaluated in non-karstic and/or confined aquifer environments as well as in systems undergoing inelastic deformation. Furthermore, the poroelastic model presented here neglects horizontal strains within the aquifer layers which may be more important in confined systems. We also recognize that the signals we attribute to poroelastic origins may be contaminated by other sources of seasonal signals, either due to deformation from thermal, atmospheric and residual hydrological loading effects or to systematic errors in the GRACE and GNSS data processing. Chanard et al. (2020) report draconitic signals, aliasing from mismodelled tides, tropospheric delays and other environmental effects as potential sources of seasonal noise and systematic errors in GNSS datasets. Perhaps most importantly, our work suggests that horizontal poroelastic displacements are highly sensitive to spatial variations in groundwater, making it difficult to accurately extract them from GNSS time series without a sufficient resolution of the piezometric surface.

Future work will thus focus on characterizing the horizontal deformation field that would help identify possible local effects in the vicinity of groundwater monitoring wells using InSAR displacement time series. Accurately measuring aquifer deformation is essential to understand its mechanics at the system scale, which is not possible from piezometric monitoring alone given the hydromechanical couplings involved. In particular, a more complete characterization of surface horizontal displacements should lead to an improved understanding of how water is stored in the different aquifers units of the Ozark system (confined-unconfined) as well as their connections.

721

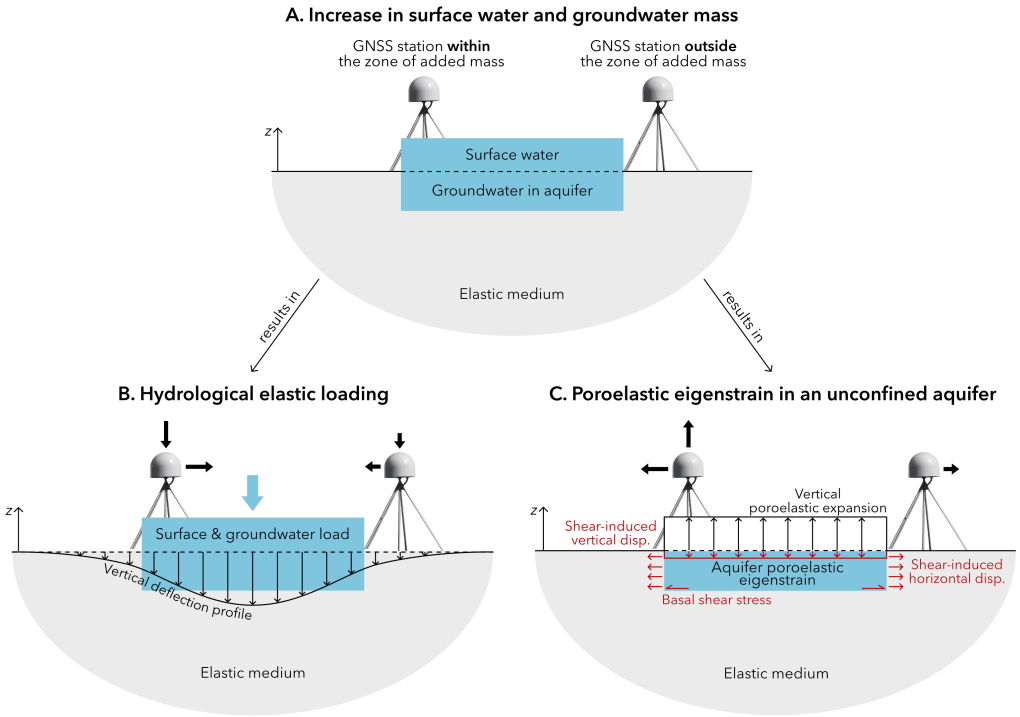

Figure 1: Deformation due to hydrological elastic loading vs poroelastic eigenstrain. A. Schematic representation of an increase in surface and groundwater mass in the vicinity of GNSS stations. **B.** The added mass, whether at the surface or in the ground, causes subsidence and horizontal motion towards the added load. The surface vertical displacement expected from a circular load on an elastic half-space is shown in black. **C.** At the same time, groundwater recharge increases pore water pressure within the aquifer, leading to upward vertical and outward horizontal displacements. While most of the vertical deformation comes from poroelastic expansion (black), horizontal and vertical displacements also result from basal shear stresses (red).

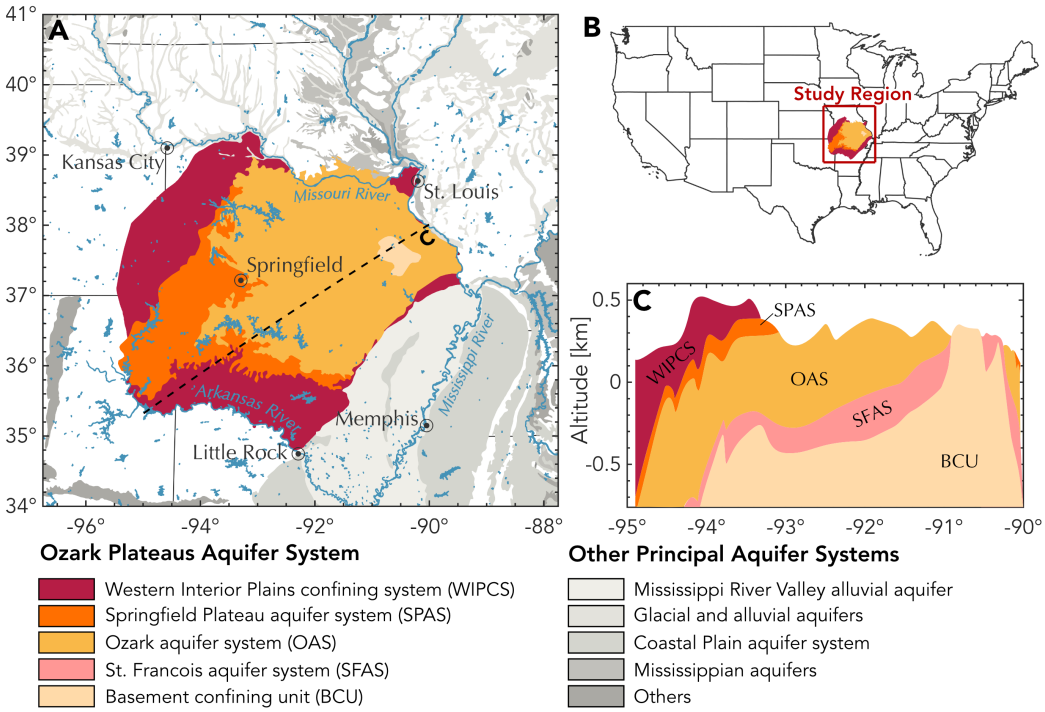

Figure 2: Regional hydrogeological setting. **A**. Simplified outcrop map of the Ozark Plateaus Aquifer System (OPAS) based on physiographic sections (modified from Hays et al. (2016) and Knierim et al. (2017)) and neighbouring aquifer systems (from USGS map of Principal Aquifers). **B**. Geographical location of OPAS. **C**. Hydrogeological cross-section at the dashed line in A based on Westerman et al. (2016).

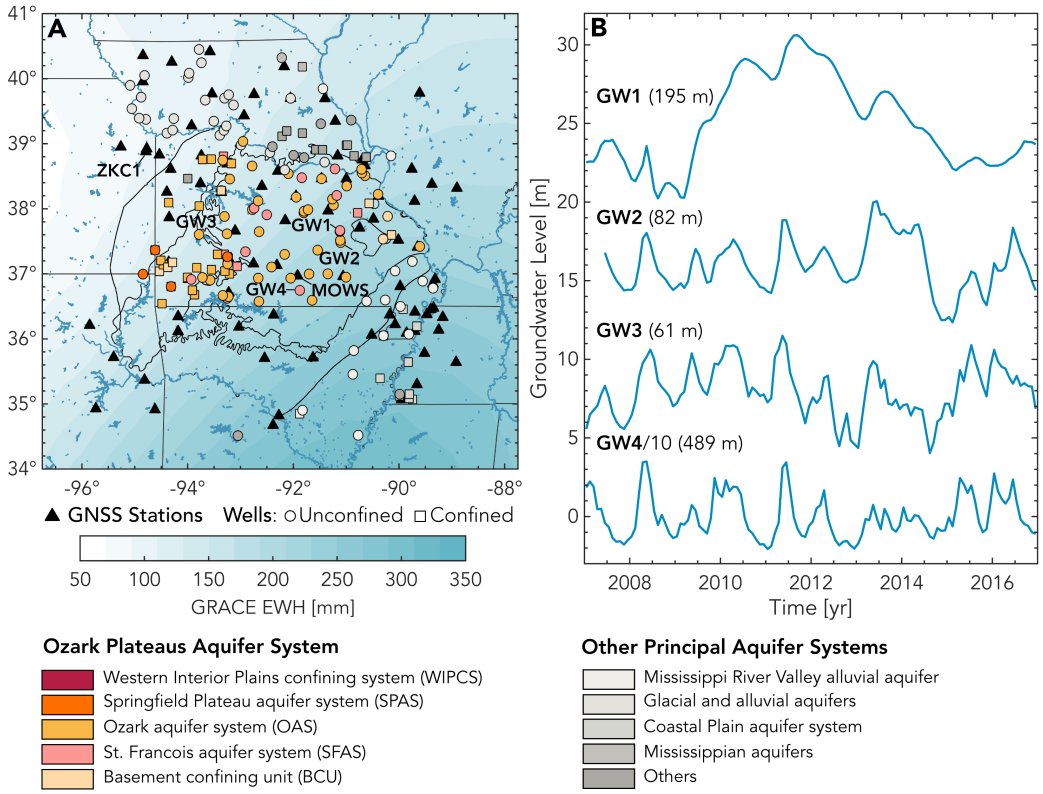

Figure 3: GNSS, GRACE and groundwater data sets. A. Annual EWH peak-to-peak amplitudes derived from GRACE and locations of GNSS stations and groundwater monitoring wells used in this study. The color of the well markers indicates the aquifer system at the base of a well and the shape describes the type of aquifer(s) - i.e., confined or unconfined - encountered by a well (as classified by the USGS). **B**. Example of groundwater time series at different locations across OPAS. Note that the time series are offsetted and that GW4 is divided by a factor of 10 for illustration purposes. Well depths are indicated in parenthesis. The featured wells correspond to USGS site numbers 373955091065901 (GW1), 372853091061801 (GW2), 373701093151601 (GW3) and 364324091515001 (GW4).

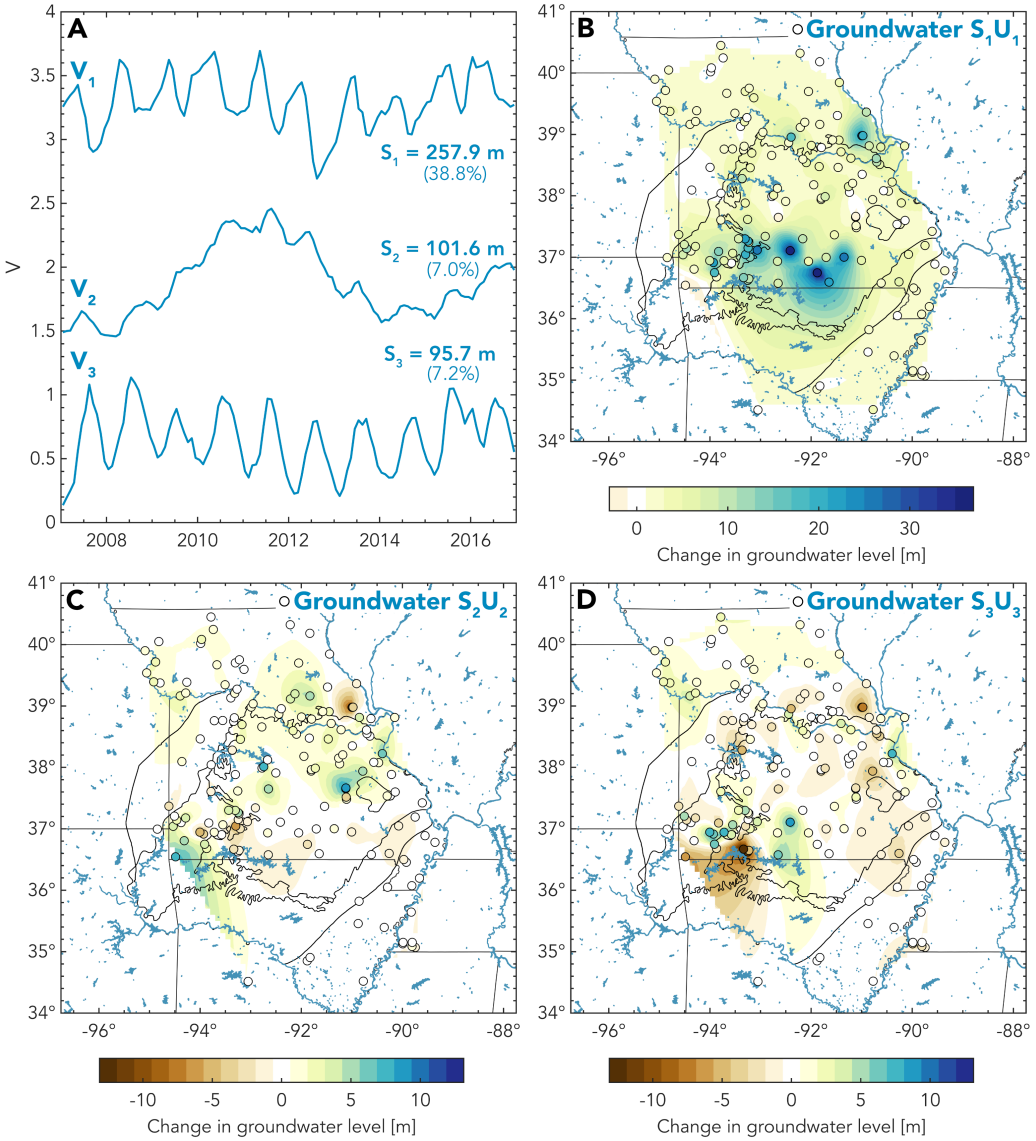

Figure 4: ICA decomposition of the groundwater dataset. A. Temporal evolution and weighting factors of the three components ICA. The temporal functions are offsetted for illustration purposes. The variance of the groundwater dataset explained by each component is also indicated in parenthesis. **B-D** Weighted spatial distributions of the three components (circles). Spatial interpolation of the distributions is also shown.

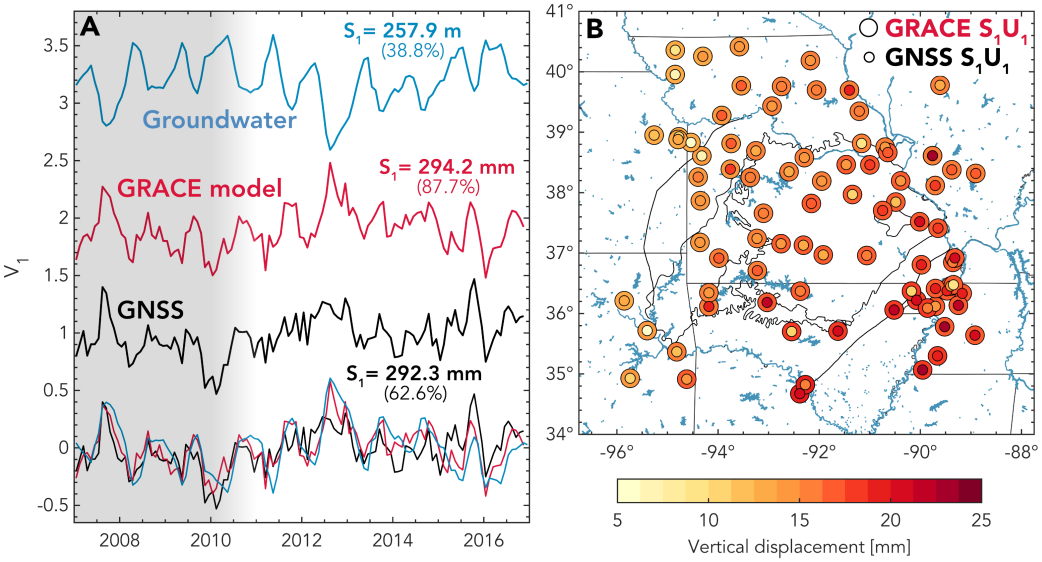

Figure 5: Temporal correlation between the first independent component of groundwater and the GRACE-predicted and GNSS vertical displacements. A. Temporal functions (offsetted), weighting factor and variance explained for each dataset. The 3 temporal functions are replotted at the bottom of the figure (note that the groundwater function is flipped) to facilitate visual comparison. The grey shaded area indicates the timespan prior to the installation of most GNSS stations sitting on top of OPAS from 2010 to 2011. **B.** Spatial distribution of the GRACE-predicted (outer circles) and GNSS (inner circles) vertical displacement datasets.

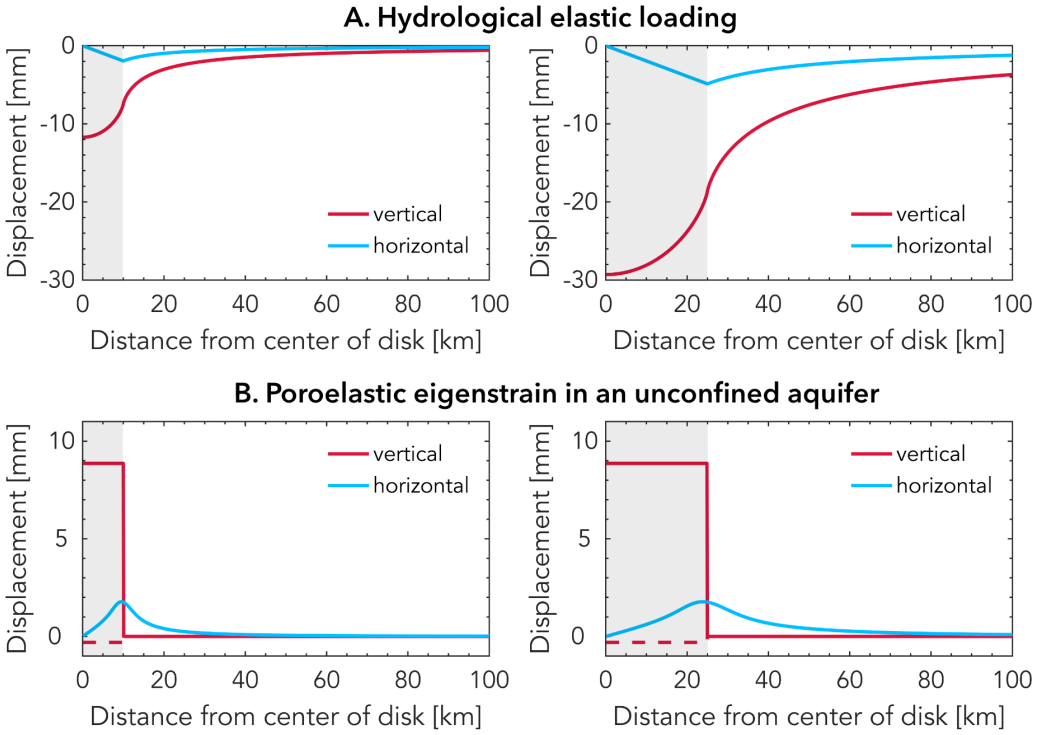

Figure 6: Surface displacements due to hydrological elastic loading vs poroelastic eigenstrain. Vertical and horizontal surface displacements induced by **A**. a disk load at the surface of an elastic half-space and **B.** poroelastic eigenstrain in a circular unconfined aquifer as illustrated in Figure 1 for disks of radius $a = 10$ km (left) and $a = 25$ km (right) as indicated by the grey-shaded areas. For the vertical poroelastic deformation, the dashed line represents the shear-induced deformation while the solid line represents the total poroelastic displacement. The increase in surface water level, P, and groundwater level, Δh, are set at 5 and 20 m, respectively, consistent with a 25% porosity. Other parameter values are: $\nu = 0.25$, $E_{deep} = 80$ GPa, $E_{aq} = 10$ GPa, $\beta = 0.8$, $b = 1000$ m.

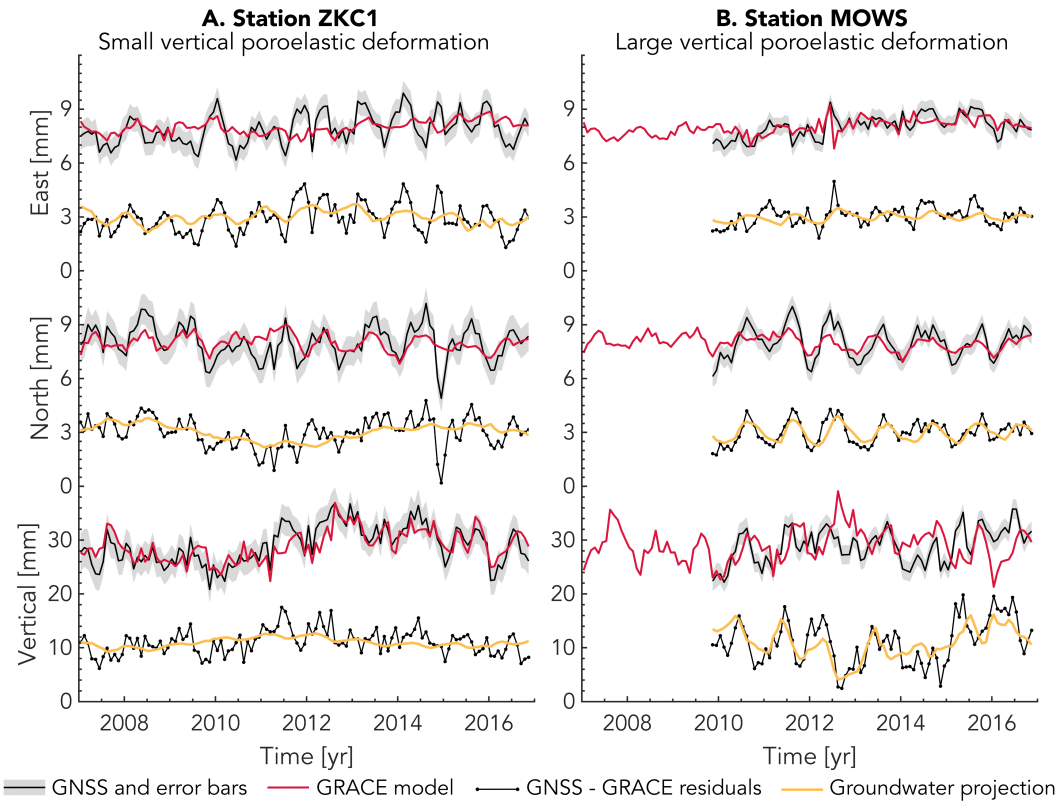

Figure 7: Extracting the OPAS's poroelastic signal from GNSS time series. Black lines with grey error bars are GNSS time series (corrected for degree 1). A common mode has been removed in the East and North components. Red lines are the GRACE model predictions. Black dots are the GNSS-GRACE residuals. Yellow lines are the projection of the GNSS-GRACE residuals onto the W_i from the groundwater ICA.

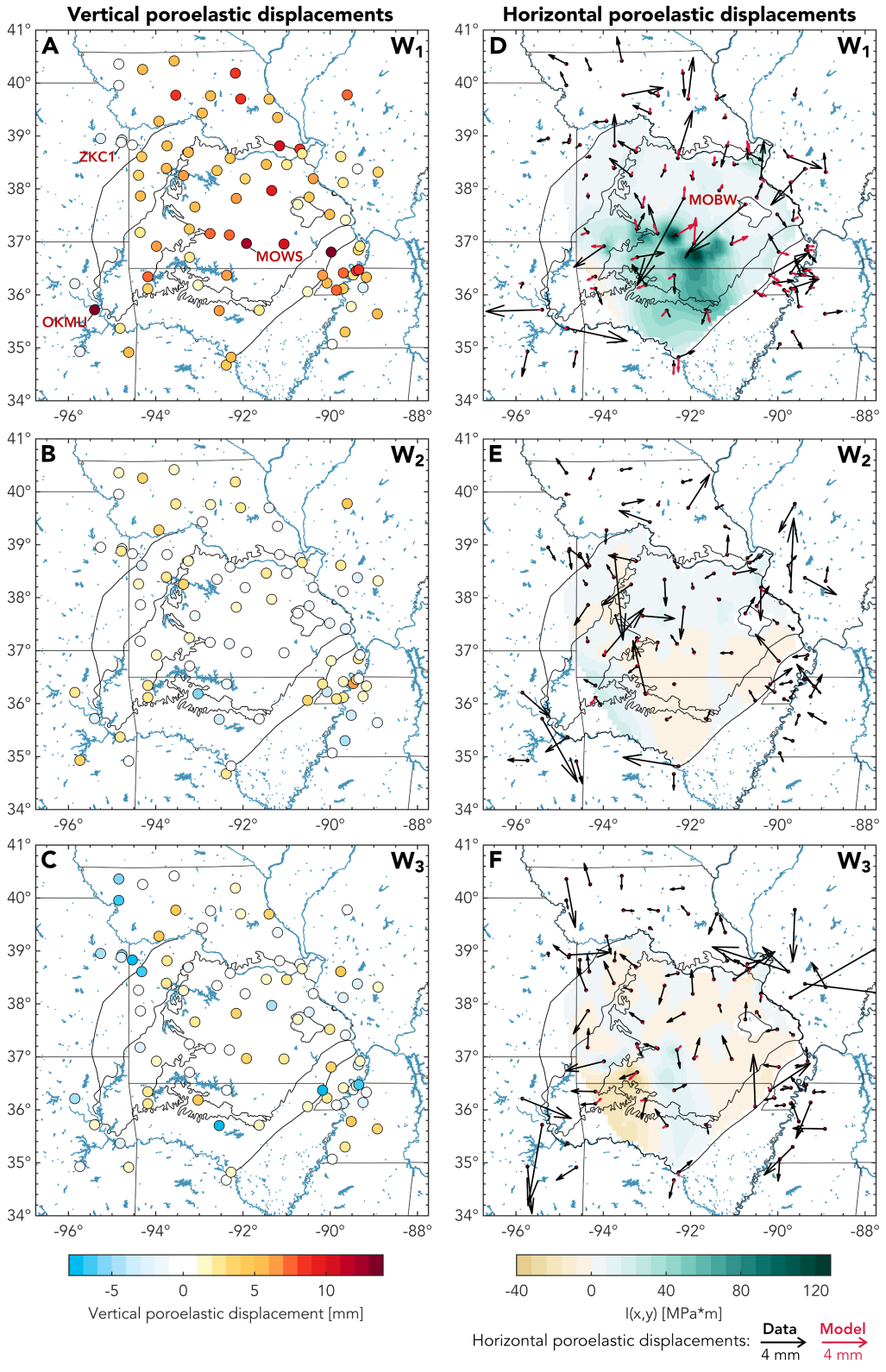

Figure 8: Inferred poroelastic displacements and model predictions of poroelastic horizontal displacements. Vertical (A-C) and horizontal (D-F) poroelastic displacement extracted by projecting onto the different temporal functions W_i. **D-F.** Distribution of $I(x, y)$ from each groundwater IC and resulting horizontal poroelastic displacement (red arrows).

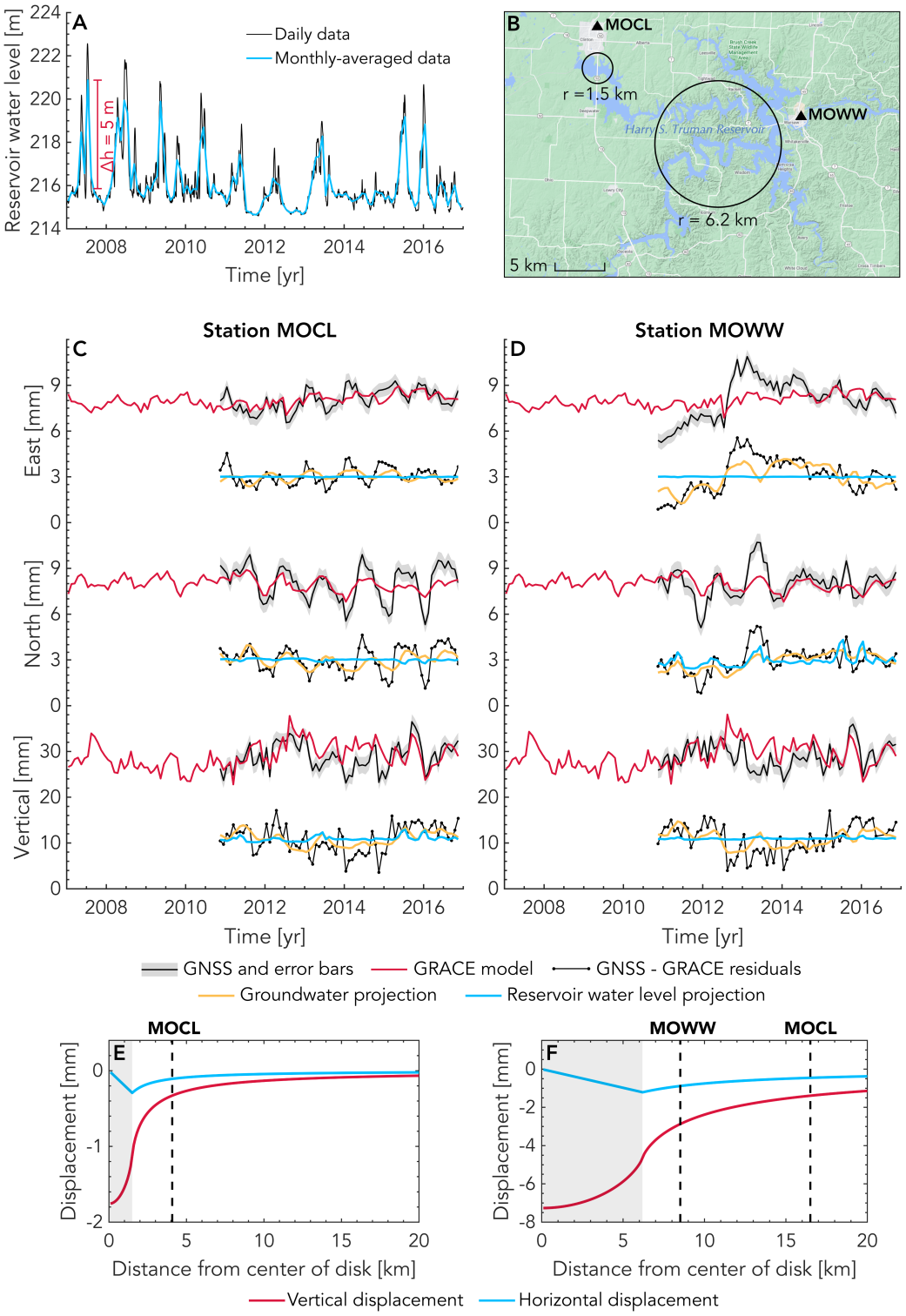

Figure 9: Estimating the elastic loading contribution from a surface water reservoir. (A) Daily and monthly-averaged temporal evolution of water levels at the Harry S. Truman Reservoir. (B) Location of GNSS stations MOCL and MOWW with respect to the reservoir. (C,D) Same as Figures 7 and S2 but with projections of the GNSS-GRACE residuals onto reservoir water levels (blue). (E,F) Displacements associated with the analytical elastic loading model (as in Figure 6A) for the circular regions shown in (B) and a 5m increase in water level.

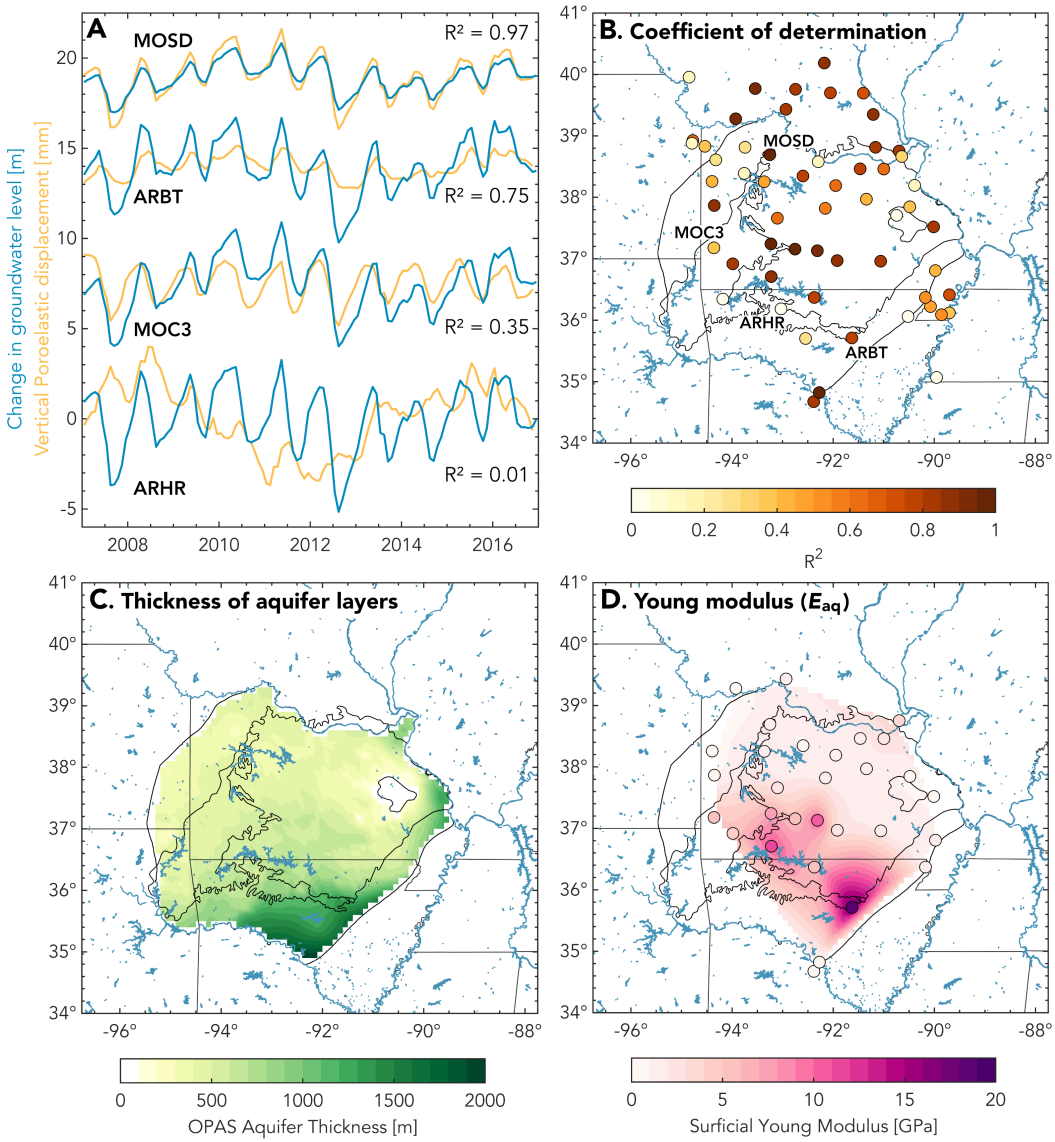

Figure 10: Estimating aquifer Young modulus from vertical poroelastic displacement and groundwater level variations A. Examples of vertical poroelastic displacement time series and groundwater level change extracted with ICA and interpolated at the GNSS stations location. Note that the time series are offsetted for illustration purposes. **B.** Coefficient of determination (R^2) of a linear fit through poroelastic displacement vs change in groundwater level. The higher R^2, the better the E_{aq} estimate. **C.** Total thickness of the aquifer layers. **D.** Young's Modulus computed for $R^2 > 0.35$ and where all three input variables are available.

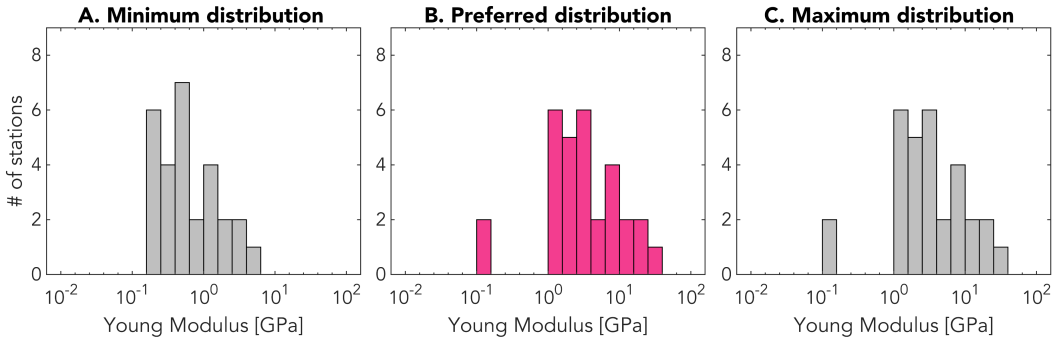

Figure 11: Inferred distributions of aquifer Young modulus. The preferred distribution (B) is computed with $\nu = 0.25$, $\beta = 0.80$, $\phi = 0.25$, and $b = b_{model}$ while the minimum (A) and maximum (C) distributions are computed with $\nu = 0.33$ and 0.25, $\beta = 0.6$ and 0.9, $\phi = 0.40$ and 0.00, and $b = b_{model} \mp 36$ m, respectively. Note that two stations were removed for the minimum distribution as the aquifer thickness becomes negative when subtracting 36 m.

Appendix A Arbitrary 2D poroelastic eigenstrains in an elastic half-space

When the 2D spatial distribution is arbitrary, quantity I defined in Equation (14) can be rewritten in Cartesian coordinates as:

$$I(x,y) = \int_0^b \frac{E_{aq}(x,y)\varepsilon_{eig}(x,y) - \nu(x,y)\sigma_{zz}(x,y)}{1-\nu(x,y)}\partial z \tag{A1}$$

We can decompose $I(x,y)$ into its Fourier components as:

$$\begin{aligned} I(x,y) \quad = \quad & \sum_{k_x,k_y} A_1(k_x,k_y)\cos(k_x x)\cos(k_y y) + A_2(k_x,k_y)\cos(k_x x)\sin(k_y y) \\ & + A_3(k_x,k_y)\sin(k_x x)\cos(k_y y) + A_4(k_x,k_y)\sin(k_x x)\sin(k_y y) \end{aligned} \tag{A2}$$

where k_x and k_y are the wavenumbers in the x and y directions. Similar to Equation (22), the horizontal displacement field can then be computed as:

$$\begin{aligned} u_x \quad = \quad & \frac{2(1-\nu^2)}{E_{deep}} \sum_{k_x,k_y} -A_1(k_x,k_y)\sin(k_x x)\cos(k_y y) - A_2(k_x,k_y)\sin(k_x x)\sin(k_y y) \\ & + A_3(k_x,k_y)\cos(k_x x)\cos(k_y y) + A_4(k_x,k_y)\cos(k_x x)\sin(k_y y) \end{aligned} \tag{A3}$$

$$\begin{aligned} u_y \quad = \quad & \frac{2(1-\nu^2)}{E_{deep}} \sum_{k_x,k_y} -A_1(k_x,k_y)\cos(k_x x)\sin(k_y y) + A_2(k_x,k_y)\cos(k_x x)\cos(k_y y) \\ & - A_3(k_x,k_y)\sin(k_x x)\sin(k_y y) + A_4(k_x,k_y)\sin(k_x x)\cos(k_y y) \end{aligned} \tag{A4}$$

Appendix B Analytical elastic loading solution for $r \to a$

Since $\mathcal{K}(k)$ in Equation (22) diverges when $r = a$, the solution diverges at $r = a$. However, we can express and evaluate the $\mathcal{K}(k)$ and $\mathcal{E}(k)$ terms with infinite series truncated for an arbitrary n to numerically approach the solution at $r = a$:

$$\left(\frac{2}{k^2} - 1\right)\mathcal{K}(k) - \frac{2}{k^2}\mathcal{E}(k) = \frac{\pi}{2}\sum_{n=0}^{\infty} \frac{n}{n+1}\left(\frac{(2n)!}{2^{2n}(n!)^2}\right)^2 k^{2n} \tag{B1}$$

Acknowledgments

The USGS groundwater level, CSR GRACE and NGL GNSS time series used in this work are available at `https://waterservices.usgs.gov`, `https://podaac.jpl.nasa.gov/dataset/GRACE_GSM_L2_GRAV_CSR_RL06` and `http://geodesy.unr.edu`, respectively. The Ozark Plateaus Aquifer System model of Westerman et al. (2016) is available at `http://dx.doi.org/10.5066/F7HQ3X0T`. This study was supported by the National Sciences and Engineering Research Council of Canada through a postgraduate doctoral scholarship (PGSD-3-517078-2018), the Office for Science and Technology of the Embassy of France in the United States through a STEM Chateaubriand Fellowship as well as the Institut de Physique du Globe de Paris (IPGP contribution #4232). The authors would like to thank the editor, Paul Tregoning, and two anonymous reviewers for their constructive comments which have led to an improved manuscript as well as Roland Bürgmann for insightful discussions. SL would also like to thank Katherine Knierim for providing helpful resources to map OPAS as well as Wilbur Shirley for help with the Fourier analysis.

References

Adusumilli, S., Borsa, A. A., Fish, M. A., McMillan, H. K., & Silverii, F. (2019). A Decade of Water Storage Changes Across the Contiguous United States From

GPS and satellite gravity. *Geophysical Research Letters*, 2019GL085370. doi: 10.1029/2019GL085370

Alghamdi, A., Hesse, M. A., Chen, J., & Ghattas, O. (2020). Bayesian Poroelastic Aquifer Characterization From InSAR Surface Deformation Data. Part I: Maximum A Posteriori Estimate. *Water Resources Research*, *56*(10), e2020WR027391. Retrieved from `https://onlinelibrary.wiley.com/doi/10.1029/2020WR027391` doi: 10.1029/2020WR027391

Altamimi, Z., Rebischung, P., Métivier, L., & Collilieux, X. (2016). ITRF2014: A new release of the International Terrestrial Reference Frame modeling nonlinear station motions. *Journal of Geophysical Research: Solid Earth*, *121*(8), 6109–6131. doi: 10.1002/2016JB013098

Amelung, F., Galloway, D. L., Bell, J. W., Zebker, H. A., & Laczniak, R. J. (1999, 6). Sensing the ups and downs of las vegas: Insar reveals structural control of land subsidence and aquifer-system deformation. *Geology*, *27*, 483. doi: 10.1130/0091-7613(1999)027⟨0483:STUADO⟩2.3.CO;2

Argus, D. F., Fu, Y., & Landerer, F. W. (2014). Seasonal variation in total water storage in California inferred from GPS observations of vertical land motion. *Geophysical Research Letters*, *41*(6), 1971–1980. doi: 10.1002/2014GL059570

Argus, D. F., Landerer, F. W., Wiese, D. N., Martens, H. R., Fu, Y., Famiglietti, J. S., ... Watkins, M. M. (2017, dec). Sustained Water Loss in California's Mountain Ranges During Severe Drought From 2012 to 2015 Inferred From GPS. *Journal of Geophysical Research: Solid Earth*, *122*(12), 10,559–10,585. doi: 10.1002/2017JB014424

Bailly, C., Fortin, J., Adelinet, M., & Hamon, Y. (2019, dec). Upscaling of Elastic Properties in Carbonates: A Modeling Approach Based on a Multiscale Geophysical Data Set. *Journal of Geophysical Research: Solid Earth*, *124*(12), 13021–13038. doi: 10.1029/2019JB018391

Barbot, S., Moore, J. D., & Lambert, V. (2017). Displacement and stress associated with distributed anelastic deformation in a half-space. *Bulletin of the Seismological Society of America*, *107*. doi: 10.1785/0120160237

Bayless, E. R., Arihood, L. D., Reeves, H. W., Sperl, B. J., Qi, S. L., Stipe, V. E., & Bunch, A. R. (2017). *Maps and grids of hydrogeologic information created from standardized water-well drillers' records of the glaciated United States* (Tech. Rep.). doi: 10.3133/sir20155105

Bell, J. W., Amelung, F., Ferretti, A., Bianchi, M., & Novali, F. (2008, 2). Permanent scatterer insar reveals seasonal and long-term aquifer-system response to groundwater pumping and artificial recharge. *Water Resources Research*, *44*. doi: 10.1029/2007WR006152

Bettadpur, S. (2018). Gravity Recovery and Climate Experiment Level-2 Gravity Field Product User Handbook. , *734*, 1–21.

Bettinelli, P., Avouac, J.-P., Flouzat, M., Bollinger, L., Ramillien, G., Rajaure, S., & Sapkota, S. (2008). Seasonal variations of seismicity and geodetic strain in the Himalaya induced by surface hydrology. *Earth and Planetary Science Letters*, *266*(3-4), 332–344. doi: 10.1016/J.EPSL.2007.11.021

Bevis, M., & Brown, A. (2014). Trajectory models and reference frames for crustal motion geodesy. *Journal of Geodesy*, *88*(3), 283–311. doi: 10.1007/s00190-013-0685-5

Blewitt, G., Hammond, W. C., & Kreemer, C. (2018). Harnessing the GPS data explosion for interdisciplinary science. *Eos*, *99*. doi: 10.1029/2018EO104623

Blewitt, G., Lavallée, D., Clarke, P., & Nurutdinov, K. (2001). A new global mode of Earth deformation: seasonal cycle detected. *Science (New York, N.Y.)*, *294*(5550), 2342–5. doi: 10.1126/science.1065328

Borsa, A. A., Agnew, D. C., & Cayan, D. R. (2014, sep). Ongoing drought-induced uplift in the western United States. *Science*, *345*(6204), 1587–1590. doi: 10.1126/

SCIENCE.1260279

Boussinesq, J. (1885). *Application des potentiels à l'étude de l'équilibre et du mouvement des solides élastiques*. Blanchard: Reprint Paris.

Calais, E., Camelbeeck, T., Stein, S., Liu, M., & Craig, T. J. (2016). A new paradigm for large earthquakes in stable continental plate interiors. *Geophysical Research Letters*, *43*(20), 10,621–10,637. doi: 10.1002/2016GL070815

Carlson, G., Shirzaei, M., Ojha, C., & Werth, S. (2020, 9). Subsidence-derived volumetric strain models for mapping extensional fissures and constraining rock mechanical properties in the san joaquin valley, california. *Journal of Geophysical Research: Solid Earth*, *125*. Retrieved from `https://onlinelibrary.wiley.com/doi/10.1029/2020JB019980` doi: 10.1029/2020JB019980

Chanard, K., Fleitout, L., Calais, E., Rebischung, P., & Avouac, J. (2018). Toward a Global Horizontal and Vertical Elastic Load Deformation Model Derived from GRACE and GNSS Station Position Time Series. *Journal of Geophysical Research: Solid Earth*, *123*(4), 3225–3237. doi: 10.1002/2017JB015245

Chanard, K., Métois, M., Rebischung, P., & Avouac, J.-P. (2020). A warning against over-interpretation of seasonal signals measured by the Global Navigation Satellite System. *Nature Communications*, *11*(1), 1375. doi: 10.1038/s41467-020-15100-7

Chaussard, E., Bürgmann, R., Shirzaei, M., Fielding, E. J., & Baker, B. (2014). Predictability of hydraulic head changes and characterization of aquifer-system and fault properties from InSAR-derived ground deformation. *Journal of Geophysical Research: Solid Earth*, *119*(8), 6572–6590. doi: 10.1002/2014JB011266

Chaussard, E., Milillo, P., Bürgmann, R., Perissin, D., Fielding, E. J., & Baker, B. (2017). Remote Sensing of Ground Deformation for Monitoring Groundwater Management Practices: Application to the Santa Clara Valley During the 2012-2015 California Drought. *Journal of Geophysical Research: Solid Earth*, *122*(10), 8566–8582. doi: 10.1002/2017JB014676

Choudrey, R. (2002). Variational methods for Bayesian independent component analysis. *Robots.Ox.Ac.Uk*, 261. Retrieved from `http://www.robots.ox.ac.uk/{~}parg/projects/ica/riz/Pubs/thesis.ps.gz`

Craig, T. J., & Calais, E. (2014). Strain accumulation in the new madrid and wabash valley seismic zones from 14 years of continuous gps observation. *Journal of Geophysical Research: Solid Earth*, *119*(12), 9110–9129.

Craig, T. J., Chanard, K., & Calais, E. (2017). Hydrologically-driven crustal stresses and seismicity in the New Madrid Seismic Zone. *Nature Communications*, *8*(1), 2143. doi: 10.1038/s41467-017-01696-w

Domenico, P. A. P. A., & Schwartz, F. W. F. W. (1998). *Physical and chemical hydrogeology*. Wiley.

Dong, D., Fang, P., Bock, Y., Cheng, M. K., & Miyazaki, S. (2002). Anatomy of apparent seasonal variations from GPS-derived site position time series. *Journal of Geophysical Research: Solid Earth*, *107*(B4), ETG 9–1–ETG 9–16. doi: 10.1029/2001JB000573

Farrell, W. E. (1972). Deformation of the Earth by surface loads. *Reviews of Geophysics*, *10*(3), 761. doi: 10.1029/RG010i003p00761

Ferreira, V., Ndehedehe, C., Montecino, H., Yong, B., Yuan, P., Abdalla, A., & Mohammed, A. (2019). Prospects for Imaging Terrestrial Water Storage in South America Using Daily GPS Observations. *Remote Sensing*, *11*(6), 679. doi: 10.3390/rs11060679

Ferronato, M., Castelletto, N., & Gambolati, G. (2010). A fully coupled 3-d mixed finite element model of biot consolidation. *Journal of Computational Physics*, *229*. doi: 10.1016/j.jcp.2010.03.018

Fleitout, L., & Chanard, K. (2018, December). Displacements and Stresses Induced by Temperature and Poroelastic Pressure Variations in the Surficial layers for an Earth with Realistic Elastic Properties. In *Agu fall meeting abstracts* (Vol. 2018,

p. G53B-03).

Fortin, J., Guéguen, Y., & Schubnel, A. (2007, aug). Effects of pore collapse and grain crushing on ultrasonic velocities and Vp/Vs. *Journal of Geophysical Research: Solid Earth*, *112*(8). doi: 10.1029/2005JB004005

Fu, Y., Argus, D. F., & Landerer, F. W. (2015). GPS as an independent measurement to estimate terrestrial water storage variations in Washington and Oregon. *Journal of Geophysical Research: Solid Earth*, *120*(1), 552–566. doi: 10.1002/2014JB011415

Galloway, D. L., & Burbey, T. J. (2011). Review: Regional land subsidence accompanying groundwater extraction. *Hydrogeology Journal*, *19*(8), 1459–1486. doi: 10.1007/s10040-011-0775-5

Ge, S., & Garven, G. (1992). Hydromechanical modeling of tectonically driven groundwater flow with application to the Arkoma Foreland Basin. *Journal of Geophysical Research*, *97*(B6), 9119. doi: 10.1029/92JB00677

Gleeson, T., Wagener, T., Döll, P., Zipper, S. C., West, C., Wada, Y., ... Bierkens, M. F. P. (2021). Gmd perspective: the quest to improve the evaluation of groundwater representation in continental to global scale models. *Geoscientific Model Development Discussions*, *2021*, 1–59. Retrieved from `https://gmd.copernicus.org/preprints/gmd-2021-97/` doi: 10.5194/gmd-2021-97

GRACE. (2018). GRACE FIELD GEOPOTENTIAL COEFFICIENTS CSR RELEASE 6.0 Ver. 6.0 PO.DAAC, CA, USA. doi: 10.5067/GRGSM-20C06

Gualandi, A., & Liu, Z. (2021). Variational bayesian independent component analysis for insar displacement time-series with application to central california, usa. *Journal of Geophysical Research: Solid Earth*, *126*, e2020JB020845. doi: 10.1029/2020JB020845

Gualandi, A., Serpelloni, E., & Belardinelli, M. E. (2016). Blind source separation problem in GPS time series. *Journal of Geodesy*, *90*(4), 323–341. doi: 10.1007/s00190-015-0875-4

Hart, R. M., Clark, B. R., & Bolyard, S. E. (2008). *Digital Surfaces and Thicknesses of Selected Hydrogeologic Units within the Mississippi Embayment Regional Aquifer Study (MERAS)* (Tech. Rep.).

Hays, P. D., Knierim, K. J., Breaker, B., Westerman, D. A., & Clark, B. R. (2016). Hydrogeology and hydrologic conditions of the Ozark Plateaus aquifer system. *U.S. Geological Survey Scientific Investigations Report*(2016-5137), 61.

Helm, D. C. (1994). Horizontal aquifer movement in a theis-thiem confined system. *Water Resources Research*, *30*. doi: 10.1029/94WR00030

Hoffmann, L. S. G. D. L., J., & Wilson, A. (2003). *Modflow-2000 ground-water model—user guide to the subsidence and aquifer-system compaction (sub) package* (Tech. Rep.).

Hu, X., & Bürgmann, R. (2020). Aquifer deformation and active faulting in Salt Lake Valley, Utah, USA. *Earth and Planetary Science Letters*, *547*, 116471. doi: 10.1016/J.EPSL.2020.116471

Imes, J. L. (1989). Analysis of the effect of pumping on groundwater flow in the Springfield Plateau and Ozark Aquifers near Springfield, Missouri. *Water Resources Investigations Report*, *89-4079*.

Imes, J. L., & Emmett, L. F. (1994). Geohydrology of the Ozark Plateaus aquifer system in parts of Missouri, Arkansas, Oklahoma, and Kansas. *US Geological Survey Professional Paper*, *1414 D*. doi: 10.3133/pp1414d

Johnson. (1987). *Contact mechanics*. Cambridge University Press.

Johnson, C. W., Fu, Y., & Bürgmann, R. (2017). Seasonal water storage, stress modulation, and California seismicity. *Science (New York, N.Y.)*, *356*(6343), 1161–1164. doi: 10.1126/science.aak9547

King, N. E., Argus, D., Langbein, J., Agnew, D. C., Bawden, G., Dollar, R. S., ... Barseghian, D. (2007). Space geodetic observation of expansion of the San Gabriel Valley, California, aquifer system, during heavy rainfall in winter 2004–2005. *Journal of Geophysical Research*, *112*(B3), B03409. doi: 10.1029/2006JB004448

Knierim, K. J., Nottmeier, A. M., Worland, S., Westerman, D. A., & Clark, B. R. (2017). Challenges for creating a site-specific groundwater-use record for the Ozark Plateaus aquifer system (central USA) from 1900 to 2010. *Hydrogeology Journal*. doi: 10.1007/s10040-017-1593-1

Kusche, J., Schmidt, R., Petrovic, S., & Rietbroek, R. (2009). Decorrelated grace time-variable gravity solutions by gfz, and their validation using a hydrological model. *Journal of geodesy*, *83*(10), 903–913.

Larochelle, S., Gualandi, A., Chanard, K., & Avouac, J. P. (2018). Identification and Extraction of Seasonal Geodetic Signals Due to Surface Load Variations. *Journal of Geophysical Research: Solid Earth*, *123*(12), 11,031–11,047. doi: 10.1029/2018JB016607

Li, W., van Dam, T., Li, Z., & Shen, Y. (2016). Annual variation detected by gps, grace and loading models. *Studia Geophysica et Geodaetica*, *60*(4), 608–621.

Longuevergne, L., Florsch, N., & Elsass, P. (2007, 4). Extracting coherent regional information from local measurements with karhunen-loève transform: Case study of an alluvial aquifer (rhine valley, france and germany). *Water Resources Research*, *43*. Retrieved from `http://doi.wiley.com/10.1029/2006WR005000` doi: 10.1029/2006WR005000

MATLAB. (2017). *9.3.0.713579 (r2017b)*. Natick, Massachusetts: The MathWorks Inc.

Matonti, C., Guglielmi, Y., Viseur, S., Bruna, P., Borgomano, J., Dahl, C., & Marié, L. (2015, jan). Heterogeneities and diagenetic control on the spatial distribution of carbonate rocks acoustic properties at the outcrop scale. *Tectonophysics*, *638*, 94–111. Retrieved from `https://www.sciencedirect.com/science/article/pii/S0040195114005666` doi: 10.1016/J.TECTO.2014.10.020

Michel, S., Gualandi, A., & Avouac, J.-P. (2019). Interseismic coupling and slow slip events on the cascadia megathrust. *Pure and Applied Geophysics*, *176*(9), 3867–3891.

Miller, M. M., Shirzaei, M., & Argus, D. (2017). Aquifer Mechanical Properties and Decelerated Compaction in Tucson, Arizona. *Journal of Geophysical Research: Solid Earth*, *122*(10), 8402–8416. doi: 10.1002/2017JB014531

Mura, T. (1982). *General theory of eigenstrains*. Springer Netherlands. doi: 10.1007/978-94-011-9306-1_1

Ojha, C., Shirzaei, M., Werth, S., Argus, D. F., & Farr, T. G. (2018). Sustained Groundwater Loss in California's Central Valley Exacerbated by Intense Drought Periods. *Water Resources Research*, *54*(7), 4449–4460. doi: 10.1029/2017WR022250

Ouellette, K. J., de Linage, C., & Famiglietti, J. S. (2013). Estimating snow water equivalent from GPS vertical site-position observations in the western United States. *Water Resources Research*, *49*(5), 2508–2518. doi: 10.1002/wrcr.20173

Riel, B., Simons, M., Ponti, D., Agram, P., & Jolivet, R. (2018). Quantifying Ground Deformation in the Los Angeles and Santa Ana Coastal Basins Due to Groundwater Withdrawal. *Water Resources Research*, *54*(5), 3557–3582. doi: 10.1029/2017WR021978

Roberts, S., & Everson, R. (Eds.). (2001). *Independent Component Analysis*. Cambridge University Press. doi: 10.1017/CBO9780511624148

Serpelloni, E., Pintori, F., Gualandi, A., Scoccimarro, E., Cavaliere, A., Anderlini, L., ... Todesco, M. (2018). Hydrologically Induced Karst Deformation: Insights From GPS Measurements in the Adria-Eurasia Plate Boundary Zone. *Journal of Geophysical Research: Solid Earth*, *123*(5), 4413–4430. doi:

966 10.1002/2017JB015252
967 Shiklomanov, I. (1993). World fresh water resources. In P. H. Gleick (Ed.), *Water in*
968 *crisis: A guide to the world's fresh water resources.* Oxford University Press.
969 Silverii, F., D'Agostino, N., Borsa, A. A., Calcaterra, S., Gambino, P., Giuliani, R.,
970 & Mattone, M. (2019, jan). Transient crustal deformation from karst aquifers
971 hydrology in the Apennines (Italy). *Earth and Planetary Science Letters*, *506*,
972 23–37. doi: 10.1016/J.EPSL.2018.10.019
973 Silverii, F., D'Agostino, N., Métois, M., Fiorillo, F., & Ventafridda, G. (2016, nov).
974 Transient deformation of karst aquifers due to seasonal and multiyear groundwater
975 variations observed by GPS in southern Apennines (Italy). *Journal of Geophysical*
976 *Research: Solid Earth*, *121*(11), 8315–8337. doi: 10.1002/2016JB013361
977 Tapley, B. D., Bettadpur, S., Ries, J. C., Thompson, P. F., & Watkins, M. M.
978 (2004). Grace measurements of mass variability in the earth system. *Science*,
979 *305*(5683), 503–505.
980 Tsai, V. C. (2011, apr). A model for seasonal changes in GPS positions and seismic
981 wave speeds due to thermoelastic and hydrologic variations. *Journal of Geophysi-*
982 *cal Research*, *116*(B4), B04404. doi: 10.1029/2010JB008156
983 van Dam, T., Wahr, J., Milly, P. C. D., Shmakin, A. B., Blewitt, G., Lavallée, D.,
984 & Larson, K. M. (2001). Crustal displacements due to continental water loading.
985 *Geophysical Research Letters*, *28*(4), 651–654. doi: 10.1029/2000GL012120
986 Vergnolle, M., Walpersdorf, A., Kostoglodov, V., Tregoning, P., Santiago, J., Cotte,
987 N., & Franco, S. (2010). Slow slip events in mexico revised from the processing of
988 11 year gps observations. *Journal of Geophysical Research: Solid Earth*, *115*(B8).
989 Verruijt, A. (2009). Elastostatics of a Half Space. In *An introduction to soil dynam-*
990 *ics.* doi: 10.1007/978-90-481-3441-0
991 Walsh, J. B. (1965). The effect of cracks on the compressibility of rock. *Journal of*
992 *Geophysical Research (1896-1977)*, *70*(2), 381-389. doi: https://doi.org/10.1029/
993 JZ070i002p00381
994 Wang, H. F. (2000). *Theory of Linear Poroelasticity with Applications to Geome-*
995 *chanics and Hydrogeology.* Princeton University Press.
996 Westerman, D. A., Gillip, J. A., Richards, J. M., Hays, P. D., & Clark, B. R. (2016).
997 Altitudes and thicknesses of hydrogeologic units of the ozark plateaus aquifer sys-
998 tem in arkansas, kansas, missouri, and oklahoma. *U.S. Geological Survey Scientific*
999 *Investigations Report*(2016-5130), 32.
1000 Wisely, B. A., & Schmidt, D. (2010, 3). Deciphering vertical deformation and
1001 poroelastic parameters in a tectonically active fault-bound aquifer using insar
1002 and well level data, san bernardino basin, california. *Geophysical Journal In-*
1003 *ternational*, *181*, 1185-1200. Retrieved from `https://academic.oup.com/`
1004 `gji/article-lookup/doi/10.1111/j.1365-246X.2010.04568.x` doi:
1005 10.1111/j.1365-246X.2010.04568.x

1006

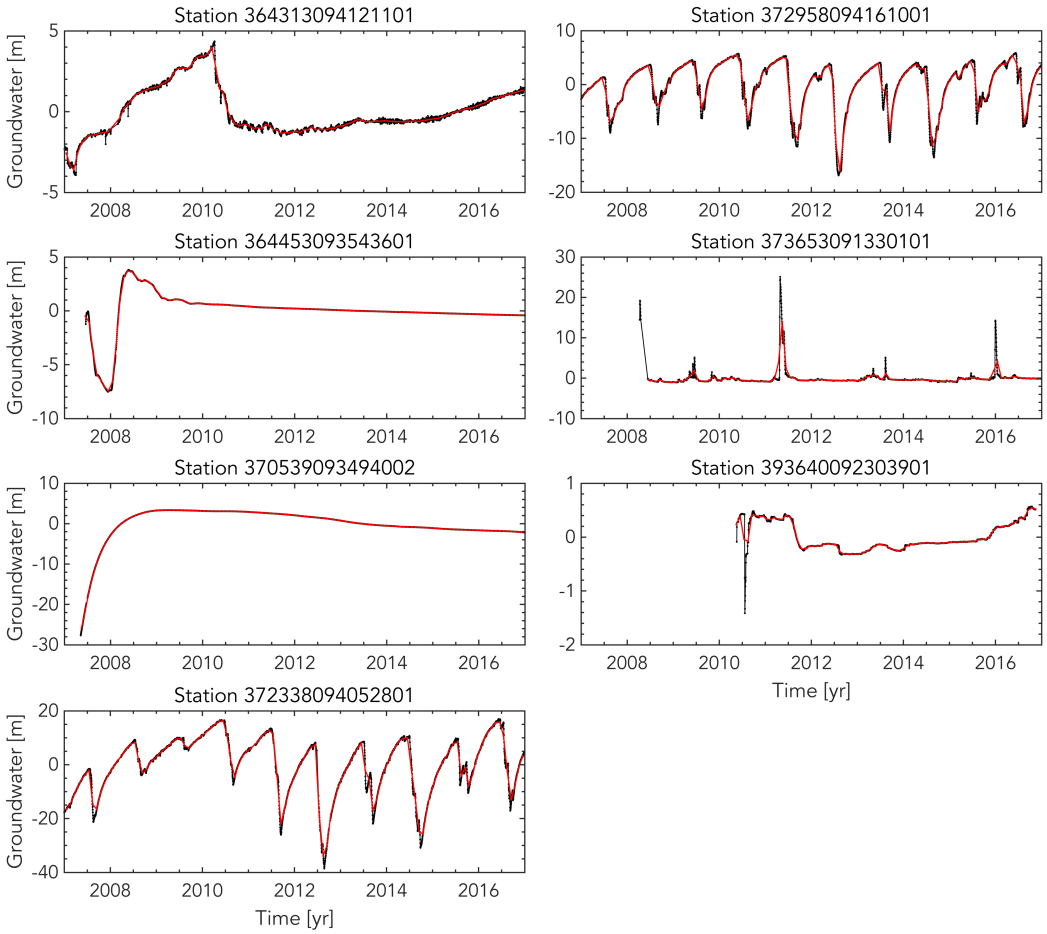

Figure S1: Groundwater time series excluded from the analysis. Black dots are the raw daily data and the red lines are the monthly averages. Stations 372958094161001 and 372338095042801 likely reflect local pumping effects.

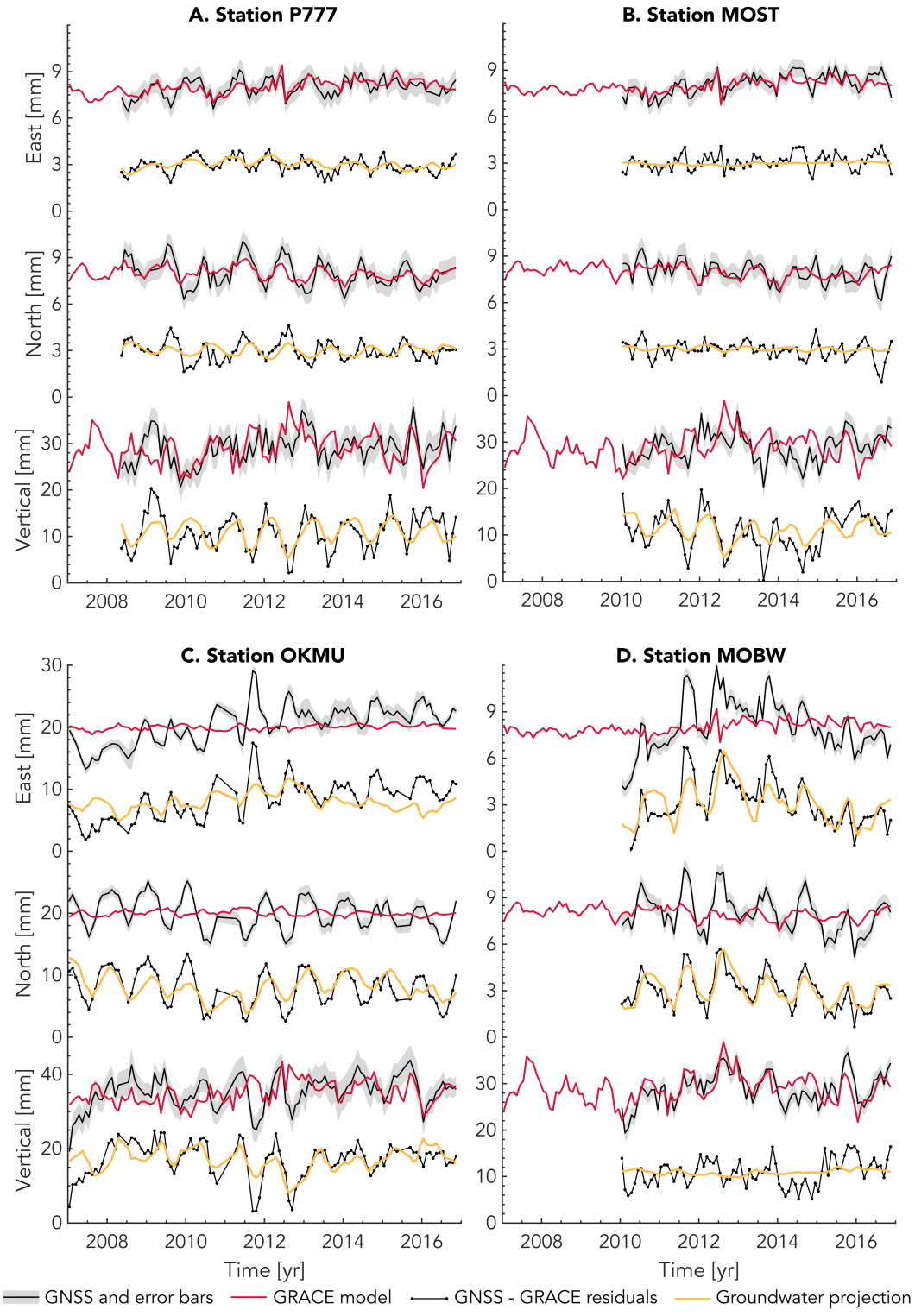

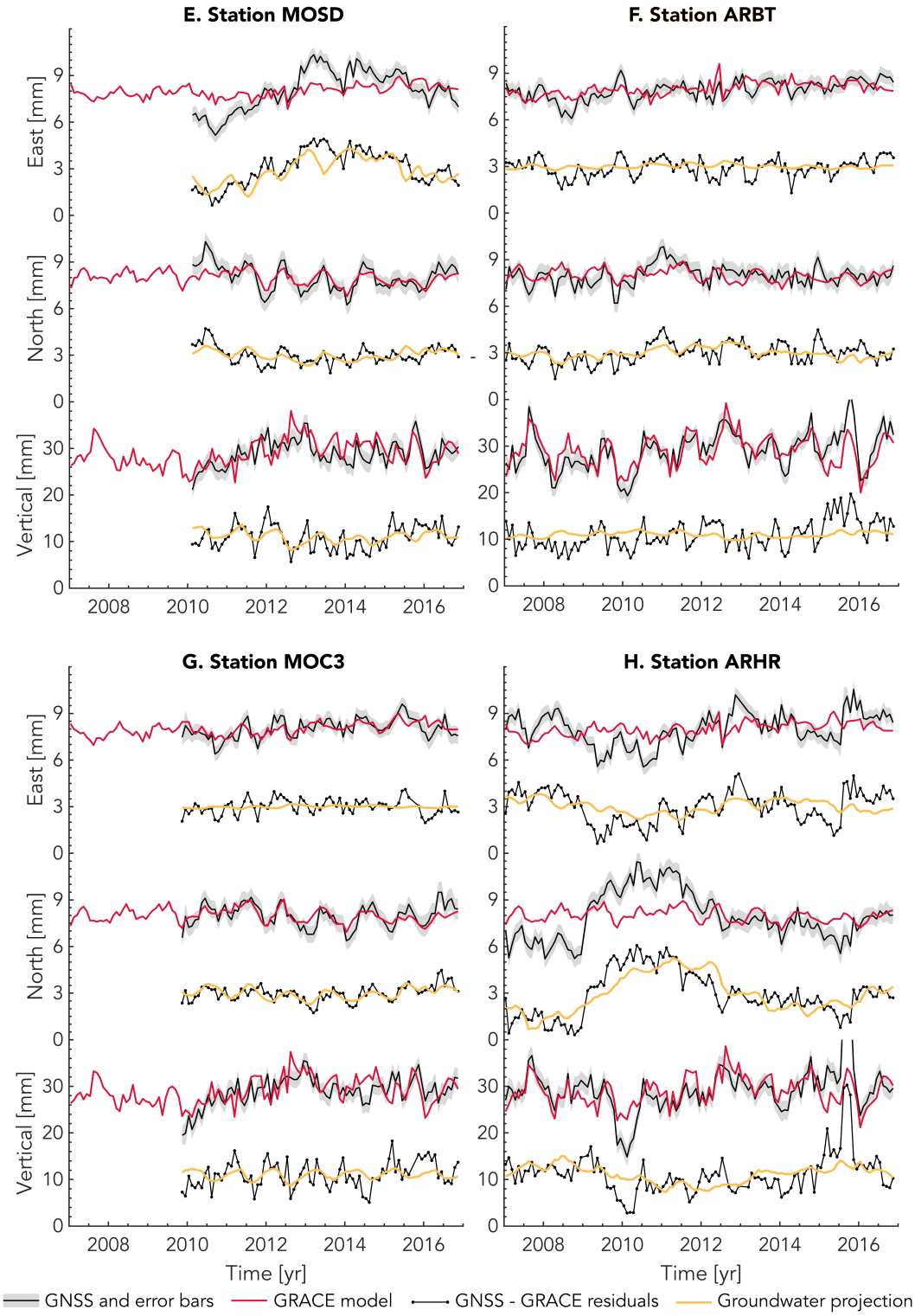

Figure S2: Additional examples of extracted poroelastic signals at different GNSS stations as in Figure 7. Note the different scales for station OKMU.

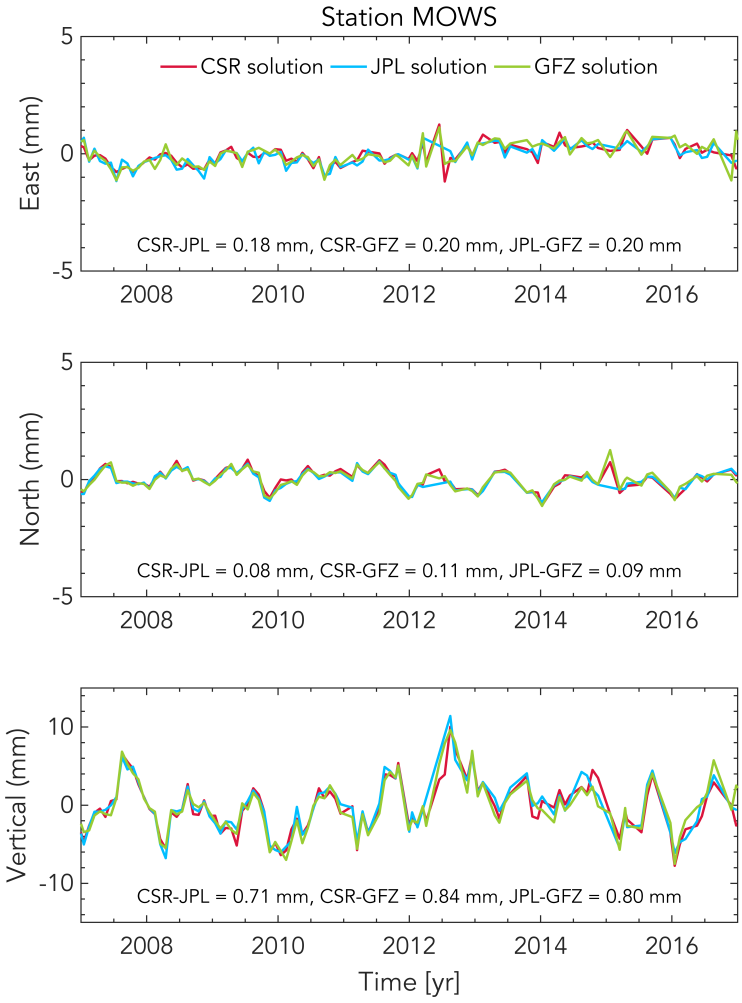

Figure S3: Modeled hydrological elastic loading displacements with different GRACE solutions. The mean absolute deviation between the different solutions are indicated in each subplot.

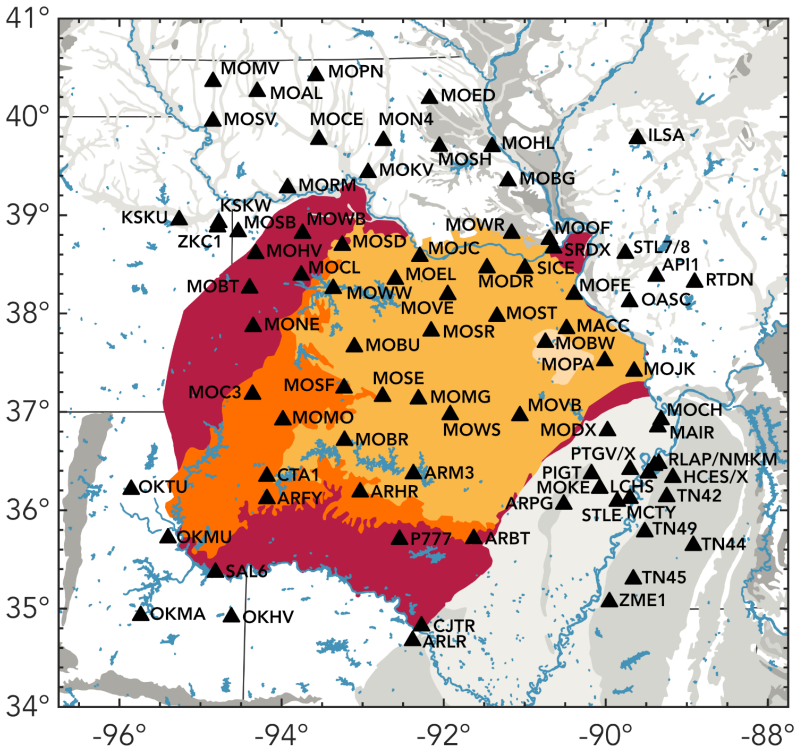

Figure S4: Names of the 86 GNSS stations retained for the analysis.

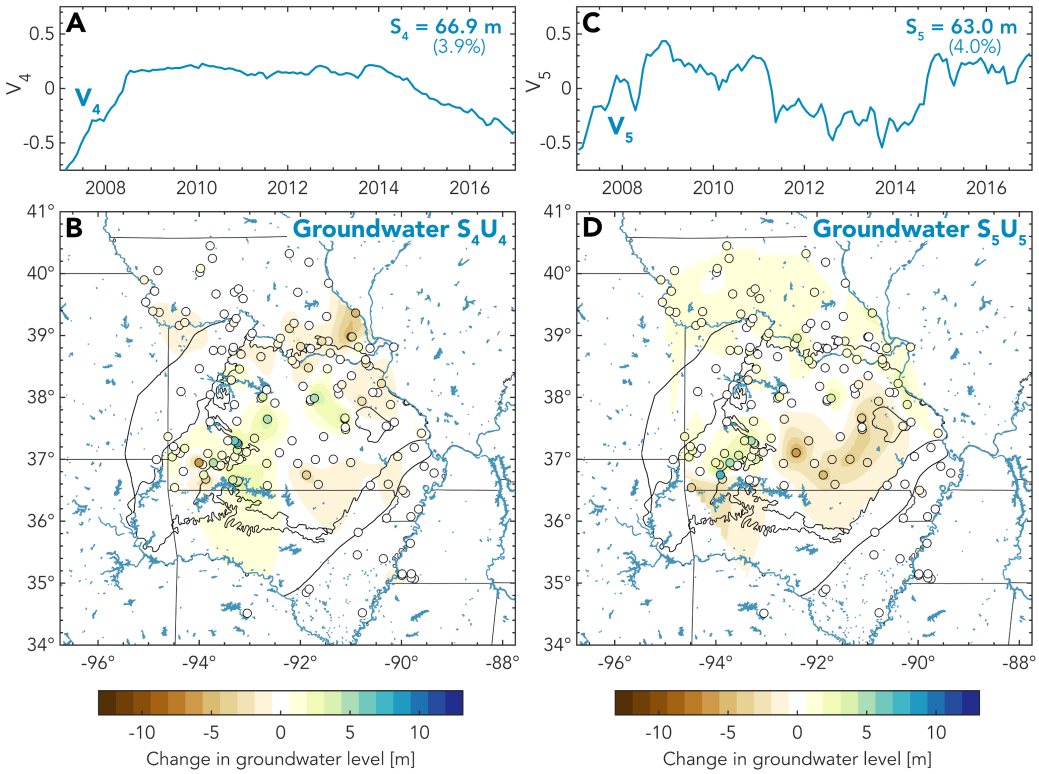

Figure S5: IC4 and IC5 of a 5-components groundwater ICA. IC1, IC2 and IC3 are similar to the 3-components ICA in Figure 5.

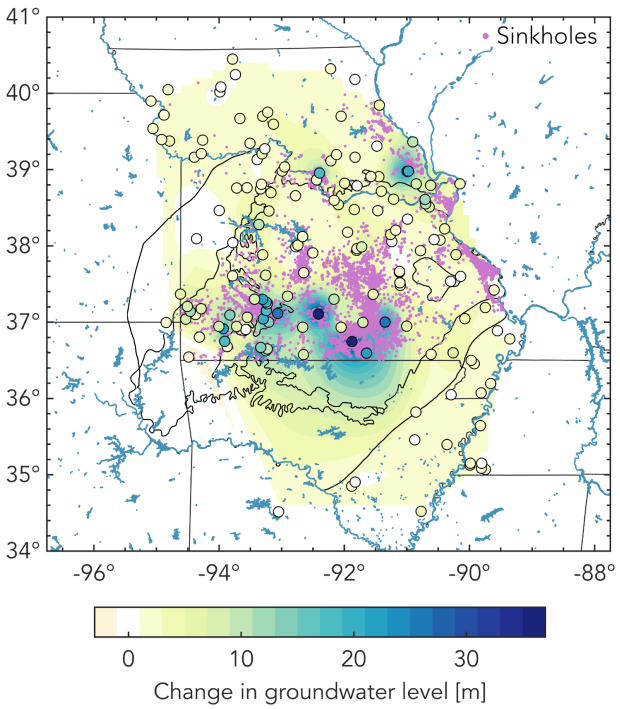

Figure S6: Comparison between the spatial distributions of sinkholes (proxy for karstification) and groundwater IC1. Purple dots indicate the location of known sinkholes in Missouri as reported by the Missouri Geological Survey (https://dnr.mo.gov/geology/geosrv/envgeo/sinkholes.htm). The spatial distribution of IC1 groundwater (same as Figure 4B) is shown for comparison.

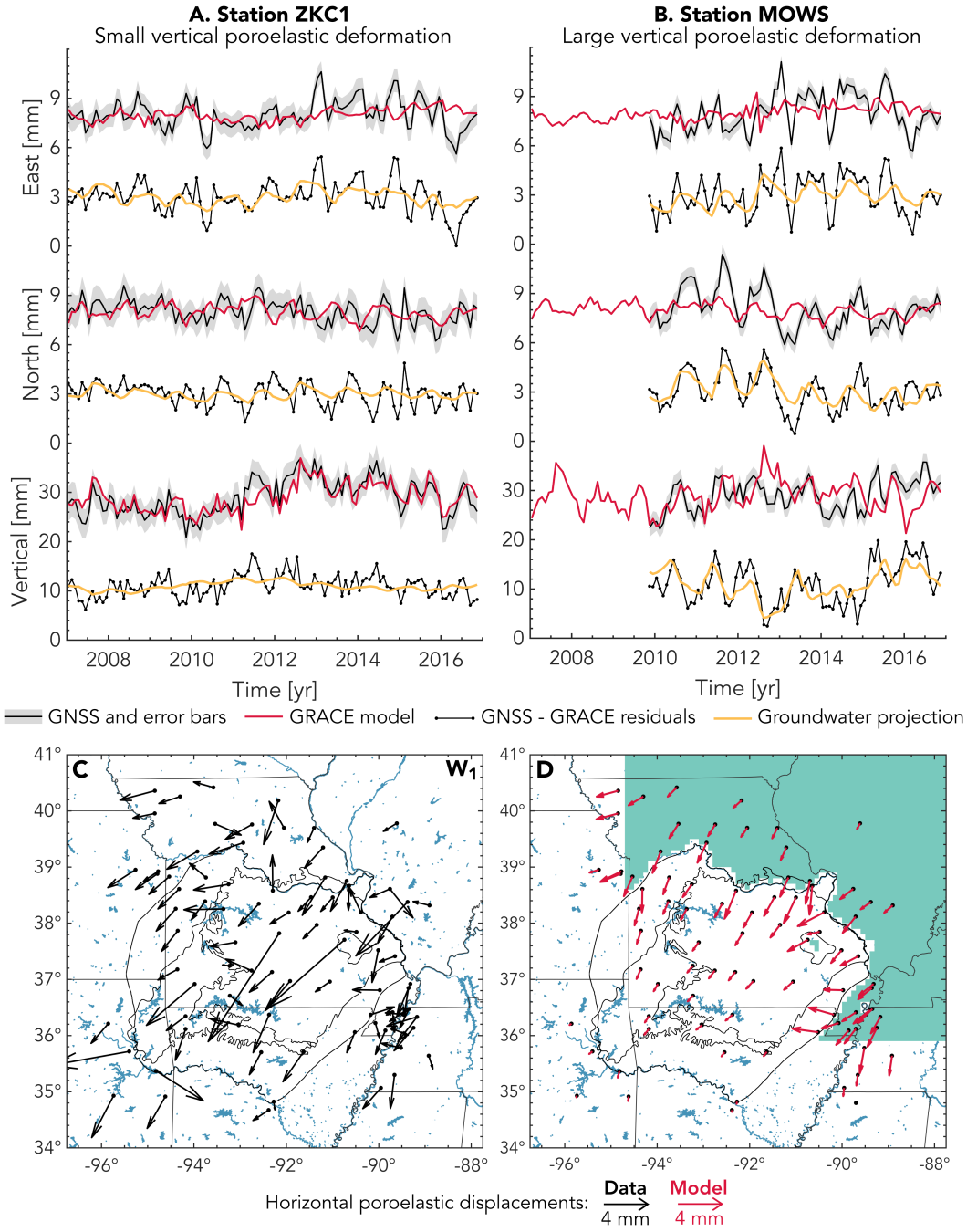

Figure S7: Common mode poroelastic signal from neighbouring aquifers. (A,B) Similar to Figure 7 but without removing horizontal common mode. (C) Horizontal poroelastic displacements inferred by projecting onto W_1 without removing common mode. (D) Modeled horizontal displacements due to poroelastic eigenstrains outside OPAS in turquoise ($\Delta h = 10$m, $b = 1000$m).

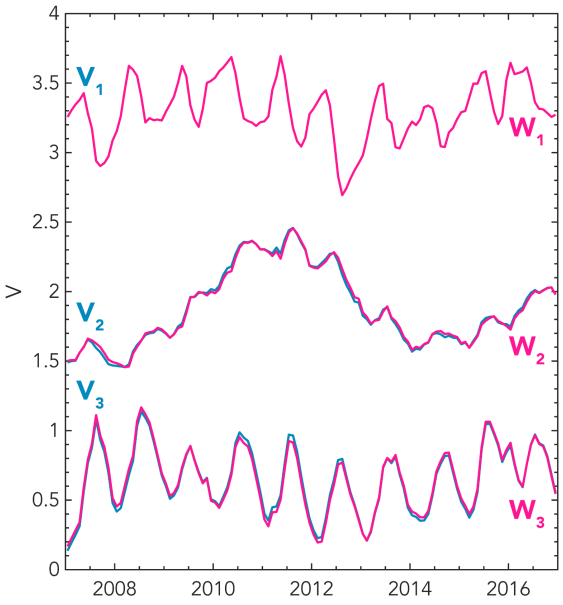

Figure S8: Original groundwater V's vs orthogonalized W's.

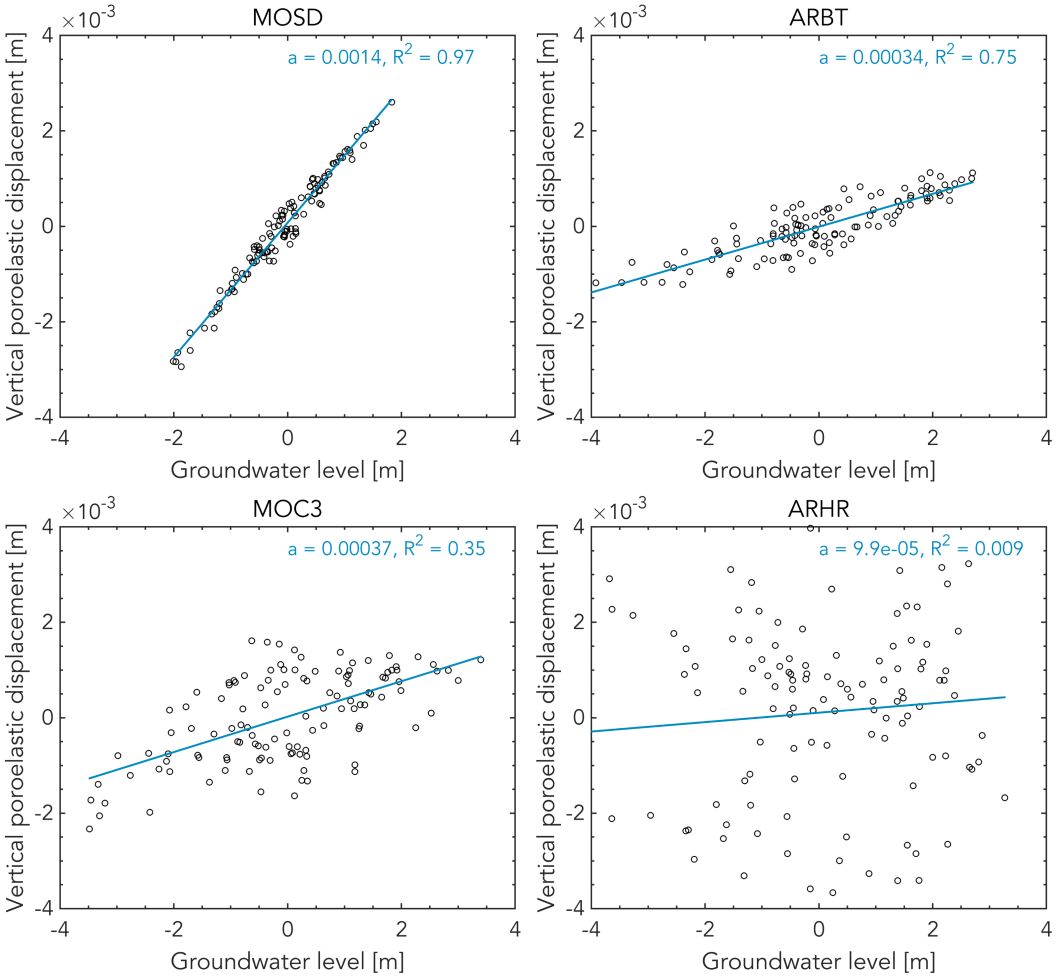

Figure S9: Coefficient of determination for stations shown in Figure 10. a is the slope of the best-fit line.

Rock	Confining stress [MPa]	Poisson ratio	Matrix bulk modulus [MPa]	Young modulus [MPa]
Blair Dolomite	0	0.25	83	125
Maxville Limestone	0	0.23	42	68
Berea Sandstone	10	0.25	6	9
Chattanooga Shale	0	0.16	5	11

Table S1: Elastic properties from Ge & Garven (1992). Note that the Young moduli were computed from the reported values of Poisson ratio and bulk modulus.